Universality in snowflake formation

by

Christopher David Westbrook

Thesis

Submitted to the University of Warwick

for the degree of

Doctor of Philosophy

Physics

December 2004

THE UNIVERSITY OF
WARWICK

Contents

List of Tables

List of Figures

Acknowledgments

Declarations

Some of the work from this thesis has been published in the following journal articles:

'Universality in snowflake aggregation' (Westbrook, Ball, Field, Heymsfield, 2004) *Geophys. Res. Lett.* **31** L15104,

'A theory of growth by differential sedimentation, with application to snowflake formation' (Westbrook, Ball, Field, Heymsfield, 2004) *Phys. Rev. E* **70** 021403,

and as a conference paper:

'A simple model of snowflake aggregation' (Westbrook, Ball, Field, Heymsfield, 2004) *Proc.* 14th *ICCP conference, Bologna.*

Also, in preparation:

'Radar scattering by aggregate snowflakes' (Westbrook, Ball, Field, 2004), to be submitted to *Quart. J. Roy. Met. Soc.*

'Is every snowflake different?' (Westbrook, Ball, Field, 2004), to be submitted to *Bull. Amer. Meteor. Soc.*

Abstract

A simple model for the formation of snowflakes in ice clouds is presented. The growth is believed to be dominated by the collision and subsequent aggregation of ice crystals sedimenting through the cloud at different speeds. The structure of the aggregates produced by this process is found to feed back on the dynamics in such a way as to stabilise both the exponents controlling the growth rate, and the fractal dimension of the clusters produced at readily predictable values. The universal features of the aggregate geometry and size distribution are identified and compared to experimental data with good agreement. Finally, the problem of interpreting radar returns from ice clouds is considered. We show that dual-wavelength radar data alone is insufficient to provide an unambiguous estimate of ice water content or precipitation rate, and that some prescription or additional measurement of the size of the snow crystals composing the aggregate snowflakes is necessary.

Chapter 1

Introduction

'Every snowflake is different', according to the well known dictum. In one sense this appears a slightly trivial statement: every blade of grass or drop of rain is different if looked at in sufficiently fine detail. Snowflakes on the other hand seem to satisfy the statement in a more fundamental way, since not only does the fine detail of the structure vary, but also the qualitative appearance of the whole flake. The snow crystals which compose them are observed to take a bewildering variety of geometrical forms, from simple hexagonal prisms to complicated dendritic shapes. These crystals aggregate with one another in a multitude of different arrangements to form the complex and varied patterns observed in the snowflakes which fall to the ground or which are sampled in aircraft flights through clouds.

Despite their apparent complexity, this thesis will attempt to demonstrate that there are features of these kind of aggregrates which are universal. These features are determined by the physical laws that govern the aggregation, and are independent of whichever of the multitude of crystal types the snowflakes are composed from, their concentration, or their distribution with size.

In this chapter, the essential ideas of ice cloud physics, aggregation and universality are reviewed, preparing the way for the construction of the model, its simulation on computer, a theoretical analysis through the scaling of the Smoluchowski equations, and finally its application to the problem of radar scattering by snowflakes. An overview of the structure of thesis, and a more detailed description

of what it aims to achieve, is given at the end of this chapter.

1.1   Ice clouds

Ice clouds are known to play a key role in meteorology, not only in terms of precipitation (Jiusto and Weickmann 1973, Bergeron 1950), but also their impact on the earth's radiation budget and global warming (Houghton 2001). Cirrus clouds alone cover around a quarter of the earth's surface at any given time, but their influence on our climate through their composition, structure and radiative properties are poorly understood (Liou 1986, Mitchell *et al* 1989, Stephens *et al* 1990).

The formation of ice clouds is a result of the cooling of moist air during its ascent in the atmosphere. As the air rises it expands adiabatically in the lower pressure, reducing in temperature as it does so. The vapour then either condenses to form liquid droplets which subsequently freeze, or is sublimed to form ice directly. Both of these ice 'nucleation' mechanisms usually require some sort of foreign particle to provide a substrate for the ice nucleus (heterogeneous nucleation - Rogers and Yau 1989). For a liquid droplet to freeze homogeneously, the statistical fluctuations in the arrangement of the water molecules must conspire to produce an ice-like structure around which the freezing may begin. In bulk ice (such as ice cubes in a domestic freezer) this is readily achieved once the temperature drops below $0°C$, but for the μm-sized drops present in clouds, spontaneous freezing only occurs at temperatures around $-40°C$. Similarly, homogeneous deposition occurs when a few molecules of water vapour form a stable 'ice embryo' by chance, which requires that the air be saturated with vapour to an unrealistic degree. In general then, ice crystals form initially through heterogeneous nucleation if the cloud is warmer than $-40°C$, where some aerosol or similar foreign matter provides a surface on which the water molecules may condense together to form an ice nucleus, around which a liquid drop may freeze, or onto which water vapour may be sublimated. For clouds colder than $-40°C$, most nucleation is homogeneous.

Once nucleation has occurred, the snow crystals proceed to grow by diffusion
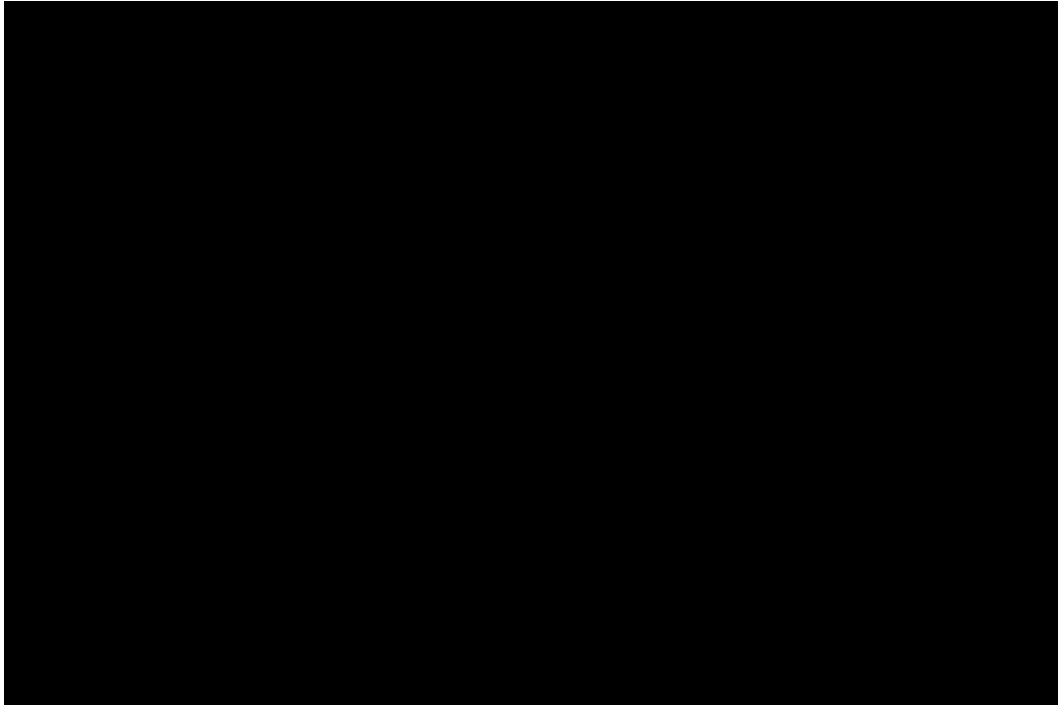
Figure 1.1: Snow crystals reproduced from Bentley and Humphries (1964), showing samples of (anti-clockwise from top left) dendrite, bullet, bullet-rosette, hexagonal column and hexagonal plate crystal types.

of the surrounding water vapour onto the ice surface. Here, the forces on the surface of the crystal govern how the water molecules are incorporated into the ice lattice, and the extent to which the crystallography influences the growth appears to vary as a function of temperature and vapour supply in a highly non-trivial way (Magono and Lee 1966). The effect of crystalline anisotropy on diffusional growth is the focus of current studies in the theoretical physics community (see section 1.3). Sample photographs from Bentley and Humphries (1964) illustrating some of the common snow crystal types are shown in figure 1.1.

As the snow crystals grow larger through diffusion they begin to fall through the cloud. Since there exist crystals with a range of shape and size, some sediment at different speeds to others, and collisions result. During such collisions the crystals may 'stick' to one another, forming aggregates (snowflakes). Figure 1.2 shows an

3

example from Jiusto and Weickmann (1973), composed of 'bullet-rosette' ice crystal types. The details of the sticking mechanism itself remain a subject of controversy in the meteorological literature (Pruppacher and Klett 1997), although suggestions include the existence of a liquid-like layer on the surface of the ice, pressure melting during the impact, and even simple mechanical interlocking in the case of dendritic crystal types.

Aggregate snowflakes are the most common type of ice particle in all but the thinnest ice clouds (Jiusto and Weickmann 1973) and aggregation is in general thought to be the dominant growth mechansim for large ice particles (Field 1999). Despite their ubiquity, aggregates are often ignored in theoretical studies on account of their highly irregular structure. Since there is such a wide variety of 'pristine' snow crystal types, attempting to categorise or quantify the geometry of aggregates appears not to be viable. They may be composed of any number of crystals, stuck together in any arrangement. A few studies have attempted to model the evolution of snowflake size distributions numerically (Passarelli and Srivastava 1979, Sasyo and Matsuō 1985), but these presume fixed empirical relationships between the snowflake mass and its radius, fall speed and collection efficiency, and do not account for the feedback between the distribution and the geometry of the aggregates. In this thesis, we study a simple theoretical model which is independent of such assumptions, and allows one to predict details of both the shape and size distribution of the aggregate snowflakes. Indeed we show in chapter three that the feedback between the geometry and the size distribution is crucial to the evolution of the aggregation and the exponent characterising their shape.

In addition to growth through collisions with one another, snowflakes may (depending on cloud conditions) also grow through riming, the accretion of super-cooled water drops lying in their path. A further complication is that the snowflakes may fracture on impact with one another, inhibiting the growth of larger flakes and increasing the population of smaller ones. For simplicity, and because of the difficulty in quantifying their effect, we neglect these processes and consider only non-destructive collisions between the snowflakes themselves. In such a regime the
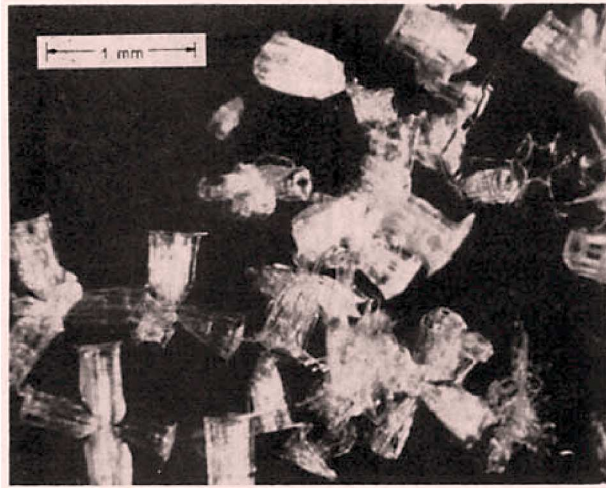
Figure 1.2: Photograph of an aggregate snowflake composed of bullet-rosette ice crystals, reproduced from Jiusto and Weickmann (1973).

growth has a number of universal features, which we attempt to identify. One such feature relates to the geometry of the snowflakes, which we find to be statistically self-similar (as described below) and characterised by a universal exponent.

1.2 Self-similarity and fractal geometry

Common experience suggests that (on the length scale of everyday experience at least) nature favours the formation of rough, irregular shapes rather than smooth, regular ones. Well known examples include coastlines (Richardson 1961); dendritic solidification, such as alloys and snow crystals (Langer 1980); the distribution of galaxies (Lucchin 1986); soot aggregates (Forrest and Witten 1979) and lightning patterns (Niemeyer *et al* 1984).

A common feature of the examples highlighted above is the qualitative similarity between the overall shape of the pattern and a small part of it. In fact the statistics of the spatial correlations in the pattern are found to be similar across a wide range of length scales, leading to the term 'statistical self-similarity'. This property is characterised by a power law scaling in the correlations between differ-

ent parts of the pattern. Consider the case of the soot aggregate: the probability density of finding a pair of particles separated by a distance Δ is well described by the scaling:

$$P(\Delta) \sim \Delta^{d_f - 3}. \tag{1.1}$$

The exponent d_f is the 'fractal dimension' of the aggregate, in this case $\simeq 2.6$. Essentially, the probability P characterises the correlation between the density at two points in the aggregate as a function of their separation Δ. For an object with uniform density P is simply a constant ($d_f = 3$); the observed power law decay of P with Δ in the case of these aggregates describes the tendency for the soot particles to cluster together rather than spread out uniformly through the space. The exponent d_f (which governs the degree to which this clustering occurs) remains constant over a wide range of length scales, indicating that clustering occurs on a similarly wide range of scales and crucially, to the same degree. Because of this, a power law decay in P is associated with self-similarity or 'fractal' geometry, where the structure of a small part of the aggregate is simply a scaled-down version of the overall cluster shape. The exact details may be different (unlike 'deterministic' fractals - Vicsek 1989), but the statistics describing the structure should be the same.

Real aggregates must of course deviate from this idealised behaviour to some degree. The particles composing the aggregate will have correlations governed by their own geometry; similarly on length scales close to the overall aggregate diameter the scaling must also break down. However, on scales larger than the size of the monomer particles but smaller than the size of the complete aggregate, the $\Delta^{d_f - 3}$ scaling is a good approximation.

Because of the scaling of the aggregate density described above, a power-law relationship between aggregate mass m and characteristic radius r is a natural expectation, specifically:

$$m = a r^{d_f}. \tag{1.2}$$

The prefactor a contains the information relating to the monomer particles which make up the aggregate, and is given by $a = \gamma m_0 / r_0^{d_f}$, where m_0 and r_0 are a characteristic monomer mass and radius respectively, and γ is a dimensionless parameter

which depends on the monomer shape. For objects of uniform density (a homogeneous sphere for example) we expect $d_f = 3$ and so $m \sim r^3$. For fractals, we expect $d_f < 3$; the lower d_f, the more inhomogeneously the composing monomers distribute themselves across the aggregate, leading to increasingly open, tenuous structures.

If the fractal dimension falls below two, then the structure becomes so open that not only does its volume not uniformly fill the space which it occupies, its projection does not fill the plane uniformly either. As a result, the projected area A scales as:

$$A \sim \begin{cases} r^2 & \text{for } d_f \geq 2 \\ r^{d_f} & \text{for } d_f \leq 2. \end{cases} \tag{1.3}$$

The projected area of fractals with a dimension of two or less then is proportional to their mass, rather than r^2. This has a number of physical implications: the drag on an aggregate falling through a fluid for example, depends on the ratio A/r^2 as discussed in the next chapter.

1.3 Review of fractal aggregation models

The recognition that aggregates of solid particles are self-similar motivated interest in theoretical models of aggregation, the most well-known of which is the diffusion-limited aggregation model (DLA) proposed by Witten and Sander (1981, 1983): their original paper has been cited over two thousand times in the literature to date. In their model a particle is released some distance away from the cluster and diffuses around until it comes into contact with it. The particle then sticks to the cluster and becomes part of it. It is well known (Mullins and Sekerka 1963, Langer 1980) that smooth growth is unstable in such a regime, and any small bumps or roughnesses tend to grow preferentially by capturing more of the diffusing particles. These roughnesses develop into the tips of branches, which screen the inner structure of the cluster from the diffusing particles. The branches themselves also develop roughnesses, from which new branches grow, yielding clusters with a tenuous, dendritic structure as shown in figure 1.3. Grown in three dimensions, these
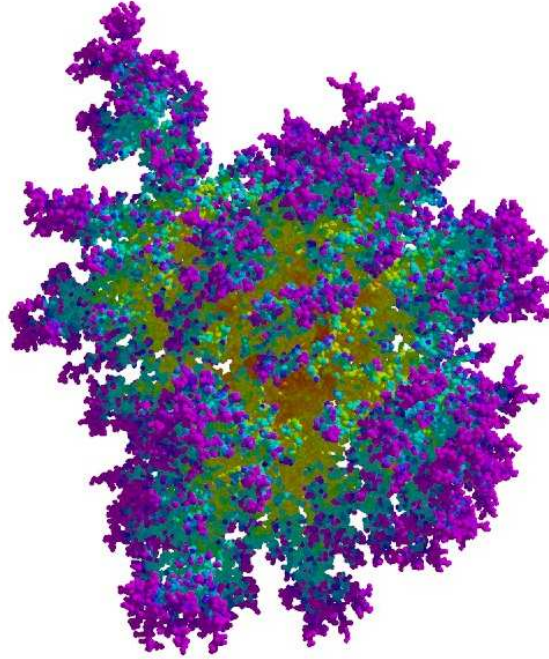
Figure 1.3: A fractal cluster grown by Goold (2004) via diffusion-limited aggregation of 10,000 spherical particles. The colours give an indication of the growth history, showing how recently the particles stuck to the cluster.

clusters are statistically self-similar, with a fractal dimension of approximately 2.5.

The DLA model, though somewhat idealised, has applications in a multitude of physical problems, in particular with regard to pattern formation in solidification. In section 1.1 it was noted that after nucleation ice crystals grow by diffusion of water vapour onto their surface. In contrast to 'standard' DLA however, the underlying atomic structure of the ice has an important effect, favouring growth along the six crystallographic directions. Recent work by Goold *et al* (2004) has investigated the effect of adding this kind of crystalline anisotropy to the DLA model, and for the case of a hexagonal lattice have produced clusters strikingly similar to the classic six-armed dendritic snowflakes of Bentley and Humphries (1964), an example of which was shown in figure 1.1.

A natural variation on the kind of models described above where particles collide and stick with a single stationary aggregate is cluster-cluster aggregation,

where the clusters themselves are allowed to move around and aggregate with one another[1]. These kinds of models have application to a wide variety of physical systems including coagulation and gelation in colloids, aggregation of aerosol particles, sedimentation of clay and other debris in rivers and oceans, the clustering of galaxies, and of course the focus of this thesis: aggregation of ice crystals to produce snowflakes. Despite the span of scientific disciplines that these examples encompass, they are fundamentally distinguished only by the physics governing the motion of the clusters, and the details of how they stick together.

The two models of cluster-cluster aggregation on which the most attention has been focussed are the cases where the aggregation is diffusion- or reaction-limited. The motion of the clusters can be Brownian in both models; the key difference between them lies in the sticking. In diffusion-limited cluster-cluster aggregation the sticking probability is unity, and the structure and kinetics are determined purely by the Brownian motion of the clusters, leading to quite tenuous, open structures ($d_f \simeq 1.8$ - Meakin 1983, Kolb *et al* 1983). In reaction-limited aggregation by contrast, the sticking probability is so low that all of the possible sticking sites on the cluster are sampled before an aggregation event takes place, leading to rather more compact structures ($d_f \simeq 2.1$ - Weitz *et al* 1985). Ballistic (straight-line) trajectories have also been considered, with Meakin (1984) finding a fractal dimension of $\simeq 1.9$. Numerous other models exist with different cluster motions, sticking mechanisms etc, but in general the clusters turn out to be fractal with a dimension universal to that physical situation and independent of the monomer details or initial distribution. In addition, the size distribution of the clusters is found be described by a universal function which is simply rescaled as the aggregation proceeds (Vicsek and Family 1984, Van Dongen and Ernst 1985). This is discussed further in section 2.3.2.

Analytical approaches to cluster-cluster aggregation have almost invariably focussed on the Smoluchowski equations (see chapter 3). Van Dongen and Ernst (1985) have used the observed universality of the size distribution to characterise the

---

[1] see Meakin (1999) for a review.

aggregation. In particular they have categorised the kinetics into a regular growth regime and run-away growth, where the largest clusters grow with ever increasing rapidity. This latter regime has been considered 'unphysical' (Van Dongen 1987a); however, the aggregation model considered in this thesis is interesting because it appears to select the marginal case between the regular growth regime and the 'unphysical' one; indeed, we show in chapter three that it is the presence of the run-away regime which forces the system to choose that state, and further allows us to directly predict the fractal dimension of the aggregates. This is very unusual: although fractal dimensions are readily inferred from computer simulations, theoretical arguments predicting d_f are usually bound up with detailed modelling of the geometry (eg. Ball *et al* 1987).

1.4   This thesis

The physics behind the growth of snowflakes in ice clouds is important, not only to quantify the precipitation from such clouds, but also to predict their radiative transfer properties. This knowledge is crucial if one seeks to accurately represent ice clouds in weather models, and to understand their effect on our climate. In addition, the interpretation of remotely sensed data from radar and satellites (which is the key to accurate forecasting) requires knowledge of the snowflake geometry and size distribution. The aim of this thesis is to construct and study a theory describing the aggregation of particles via differential sedimentation through a fluid. This kind of aggregation is believed to be the dominant mechanism by which large ice particles are produced in ice clouds, and as a result it is hoped that our theory will provide a good model for snowflake growth, allowing accurate predictions of the snowflakes' geometry and distribution by size. Models of coagulation through this mechanism are also relevant to a number of other physical systems, such as the sedimentation of clay in estuaries, and 'marine snow' formed in the ocean through the settling of dead plants, animals and other debris (eg. Kiorboe 2001).

In chapter two, the model is constructed, and simulated on computer. The

simulation results are analysed and compared with experimental data from aircraft flights through ice clouds. The results from the model prompt a new way to interpret the experimental size distributions, leading to remarkably good dynamical scaling. That scaling independently confirms that there is a single dominant growth mechanism at play. The geometry of the aggregates is studied, and is found to conform to the fractal scaling described in section 1.2. The fractal dimension is determined by the fluid flow, and is universal for a given drag regime. The aspect ratio of the clusters is also studied, and found to approach a universal asymptotic value.

In chapter three the model is simplified to allow its scaling properties to be analysed using the Smoluchowski equations. This approach highlights the fact that our aggregation model is particularly unique, on the edge of two completely different growth regimes. In fact it is the discontinuity between the two regimes which forces the system to this intermediate state. This self-organisation allows a direct prediction of the fractal dimension to be made.

Comparisons are drawn with experimental data on snowflake geometry and size distributions, with good agreement in both cases. The relationship between snowflake mass and linear span is important for meteorologists, and our model results allow the exponent linking the two to be predicted for a given fluid flow regime. In addition, the size distribution is shown to scale 'dynamically' indicating that a single universal function describes the shape of the distribution, and is merely rescaled as the aggregation proceeds as a function of the average snowflake size.

The results from the model are used in an attempt to improve the understanding of the geometry and size distribution of aggregate snowflakes, and to help clarify the interpretation of observational data. These results also have a significant impact on our understanding of the radar scattering properties of snowflakes, with implications for the methods currently used to remotely estimate microphysical quantities such as ice water content and precipitation rate, and this is considered in detail in chapter four.

11

Chapter 2

Aggregation model

Differential sedimentation is an aggregation mechanism which is relevant to several physical systems. Particles in a fluid inevitably fall through it under the influence of gravity, and since the particles are likely to have a range of sizes and shapes, the speeds at which they fall will be different, and collisions will occur. If there is some means by which the particles can stick together when they come into contact then the collisions will result in the formation of aggregates: this process is believed to be the dominant mechanism by which larger particles in ice clouds grow, as discussed in section 1.1. In this chapter, a model for aggregation by differential sedimentation in (or close to) an inertial flow regime is presented. A computer simulation based on this model has been constructed, and the results are compared to experimental data from aircraft flights through ice clouds, and from ground-based observations. A theoretical analysis of the model based on the equations of Smoluchowski (1917) follows in chapter three. The work outlined in this chapter and the next has been presented as a letter (Westbrook *et al* 2004a) and as a longer paper (Westbrook *et al* 2004b).

2.1   The Model

Ideally, we would like to model the detailed spatial and temporal evolution of the snow crystals and flakes, tracking each one individually as it falls through the cloud,

calculating where and when each collision will occur. Statistics on the geometry and size distribution of the snowflakes at various stages of the aggregation could then be collected, and the data analysed.

The achievement of this ideal is rather difficult in practice. Ice clouds are quite dilute, and as a result the number of clusters in the system must be large for significant aggregation to occur. Keeping track of the details of all the individual clusters makes analytical progress almost impossible; the practicalities of computer modelling are also significantly impaired. Not only must the position and movements of each individual cluster be recorded, requiring large amounts of computer memory, in order to find out where and when the next mutual encounter will occur, every cluster's trajectory must be checked against every other cluster's (to see which pair will collide soonest), making heavy demands on processor time. Attempting to directly model the full system then has a number of significant disadvantages, and in this thesis we attempt to construct a much simplified theory which still captures the essential physics of the problem.

We have already commented that ice clouds are dilute: according to Heymsfield and McFarquhar (2002), the typical number concentration N in mid-latitude and tropical cirrus clouds is typically no larger than 0.1cm^{-3}, and the snowflakes have a diameter D which is rarely much larger than a millimetre. The nearest-neighbour distance then is $N^{-\frac{1}{3}} \simeq 2$ centimetres. By comparison, we estimate the mean free path length to be significantly larger: $(N\pi D^2)^{-1} \simeq 3$ metres. Since the mean free path is so much longer than the nearest-neighbour separation, we make our model mean-field, and limit our interest to collision events between pairs of clusters, ignoring spatial correlation. This allows us to characterise collisions between pairs of clusters in terms of an aggregation rate which has no spatial or temporal dependence, allowing us to accurately sample collisions without the need to track every individual trajectory. As further simplifying assumptions, we assume that the clusters have random orientations which do not significantly change during a close encounter, and that all collisions result in a permanent and rigid junction.

13
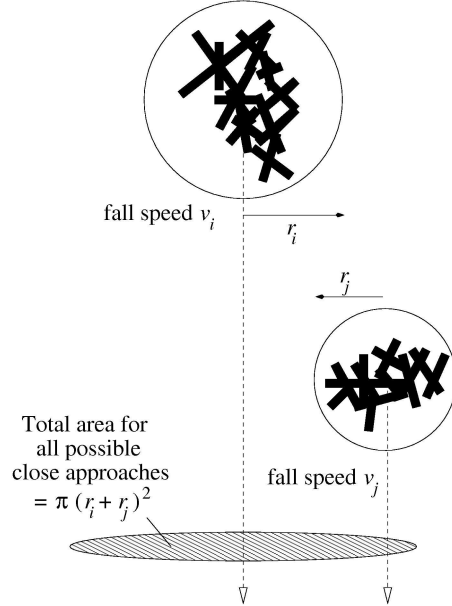
Figure 2.1: Illustration showing a possible scenario in which the centres of a pair of clusters falling at a relative speed $|v_i - v_j|$ come within a distance $(r_i + r_j)$ of one another (a close approach). The shaded circle illustrates the total area encompassing all possible close approach trajectories $= \pi(r_i + r_j)^2$.

2.1.1 Rate of close approach

To sample the collisions between pairs of clusters, a rate of close approach Γ_{ij} is calculated. For any two clusters i, j with nominal radii (see below) r_i, r_j and fall speeds v_i, v_j, the frequency with which their centres pass closer than a distance $(r_i + r_j)$ is proportional to the total area over which trajectories yielding a close approach event are possible, and the relative speed of the pair. This is illustrated in figure 2.1, and leads to the relation:

$$\Gamma_{ij} = \pi(r_i + r_j)^2 \, |v_i - v_j| \, . \tag{2.1}$$

In our computer simulations the nominal radii are chosen to fully enclose each cluster and the close approach rate calculated above is exploited to preselect candidate collision events. Collisions are accurately sampled by choosing pairs of clusters from a list with probability proportional to Γ_{ij}. A trajectory from all the possible close approaches that are encompassed by the area $\pi(r_i + r_j)^2$ is then chosen at random,

and the clusters are tracked along it to see if they do indeed collide. If they do not, the clusters are returned to the list and a new pair is picked. If a collision does occur, then they are stuck together rigidly at the point of initial contact. In our theoretical analysis (chapter three) it is assumed that all (or at least a fixed fraction of) close approaches lead to a collision.

2.1.2 Fall speeds

The model is completed by an explicit expression for the cluster fall speeds entering equation 2.1. The aerodynamic drag force on a particle is given by:

$$F_d = \frac{1}{2}\rho A v^2 C_d \tag{2.2}$$

where A is the area of the particle projected perpendicular to the flow, and ρ is the density of the surrounding fluid. The drag coefficient C_d is a function of the Reynolds number $\mathrm{Re} = rv/\nu_k$, which characterises the ratio of viscous and inertial forces in the flow[1].

The specific functional form of $C_d(\mathrm{Re})$ also depends on the shape of the particle. The results for a sphere of radius r in the viscous ($C_d = 12\mathrm{Re}^{-1}$) and inertial ($C_d = \text{constant}$) limits (corresponding to small and large Re respectively) are well known. For intermediate Reynolds numbers, Abraham (1970) argued that the flow may be divided into two regions: one close to the body where friction is important, and an outer region where it can be ignored. The drag coefficient may therefore be estimated by constructing a new 'body' Σ travelling through an inviscid fluid, where Σ = the rigid body + the boundary layer. From Tomotika's (1935) theory, the thickness of the boundary layer δ is given by:

$$\delta = r\delta_0 \mathrm{Re}^{-\frac{1}{2}} \tag{2.3}$$

where $\delta_0 = 6.40$ (McDonald 1954). The drag coefficient is then simply:

$$C_d = C_0 \left(1 + \delta_0 \mathrm{Re}^{-\frac{1}{2}}\right)^2 \tag{2.4}$$

---

[1]note that an alternative definition of Reynolds number $\mathrm{Re}' = Dv/\nu_k$ (where D is the diameter) appears in some of the literature cited here.
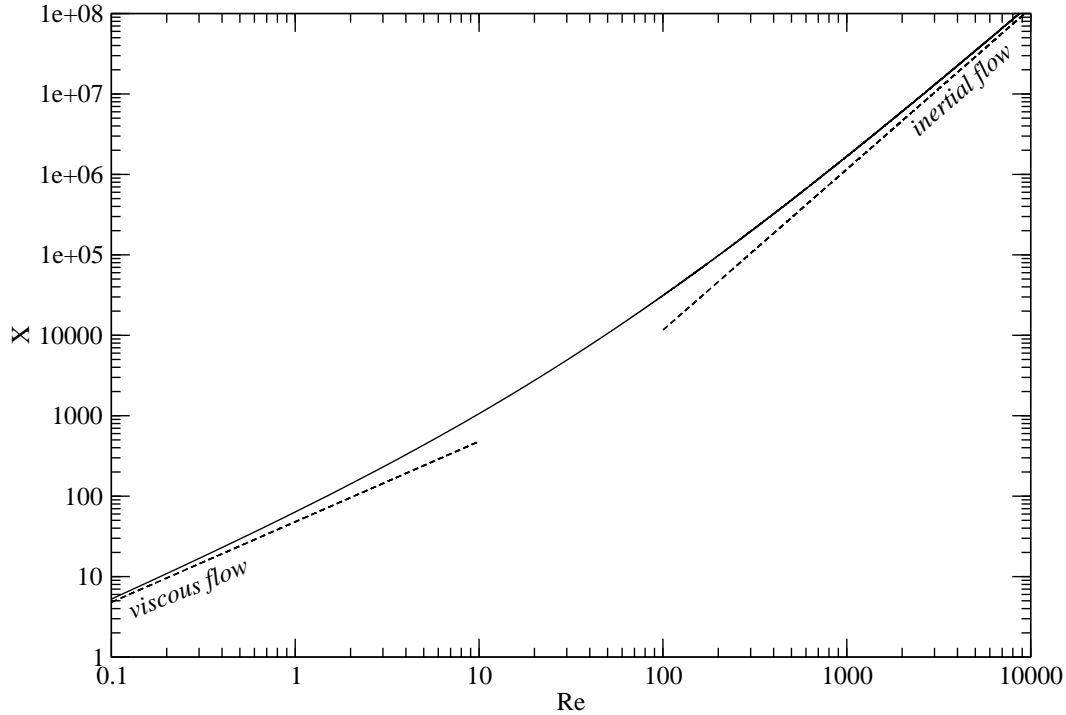
Figure 2.2: Plot of Best Number X as a function of Reynolds number Re for a rigid sphere. Solid line is derived from Abraham's expression for the drag coefficient (see text). Dashed lines show the viscous (small Re) and inertial (large Re) limits.

which is in excellent agreement with experimental data (see Abraham). The coefficient $C_0 = 0.29$ is chosen so as to match the Stokes result $C_d = 12\mathrm{Re}^{-1}$ at small Reynolds numbers.

Calculating the drag coefficient for a non-spherical particle geometry and Reynolds number is less straightforward. Mitchell (1996) resolves this by making use of empirical studies relating the Reynolds number to the Best number $X = C_d \mathrm{Re}^2$. For a sphere this relationship can be directly obtained from equation 2.4, and this is plotted in figure 2.2. For non-spherical particles, Mitchell has shown that X is well described by the same functional form, but with different constants C_0, δ_0. In any case, X(Re) takes a power law form in the inertial and viscous regimes:

$$X \sim \begin{cases} (\mathrm{Re})^2 & \text{for inertial flow} \\ (\mathrm{Re}) & \text{for viscous flow.} \end{cases} \qquad (2.5)$$

These limits are overlaid in figure 2.2. In the model presented here we consider

16

a general power law form $X \sim (\mathrm{Re})^{1/\alpha}$, with α as an adjustable parameter in an attempt to gain understanding spanning the two extremes. Mitchell shows that the crossover is quite slow (as illustrated in figure 2.2), so fixed values of α can reasonably approximate behaviour over a significant range of the X(Re) curve.

To calculate the terminal velocity, the drag force F_d is equated to the weight of the cluster mg. Knowing the relationship between $\mathrm{X} = (2mg/\nu_k^2\rho) \cdot (r^2/A)$ and $\mathrm{Re} = rv/\nu_k$ then, the fall speeds v may be directly calculated. As a simplifying assumption, we take the particles to be opaque, so that their projected area scales as $A \sim r^2$. This is justified by the results in the section 2.3 where we find that the fractal dimension $d_f \geq 2$ for all the values of α considered. Using this, and the power law relationship between X and Re, the fall speeds are given by:

$$v \sim \frac{\nu_k}{r} \left(\frac{mg}{\rho \nu_k^2} \right)^\alpha \qquad (2.6)$$

(where $\alpha = \frac{1}{2}$ for inertial flow and $\alpha = 1$ for viscous flow). The characteristic radius used to calculate v in the above expression is taken to be proportional to the radius of gyration for our computer simulations (see next section). In the theoretical analysis presented in chapter three, we make the simplification that the radius used to calculate the fall speeds scales linearly with the nominal radii used to calculate the collision cross sections.

2.2   Computer simulations

The primary particles at the beginning of the simulations were rods of zero thickness, half of which had a length (and mass) of unity, and half of which were twice as long and massive. Purely monodisperse initial conditions are not possible in this model, since $|v_i - v_j|$ would be zero. Apart from this special case however, it is anticipated that the asymptotic behaviour of the system should be insensitive to the initial distribution. Simulations were done with monomers of finite thickness and different geometry (bullet-rosette crystals, hexagonal plates), as well as for different shape initial size distributions (uniform, exponential), with no apparent effect on the results presented here, which are believed to be universal.

17

Pairs of particles are picked at random and accepted with a probability proportional to Γ_{ij}, otherwise they are returned to the list and a new pair is picked. Once a pair has been accepted, a path from the possible close approach trajectories is sampled. One cluster is positioned vertically above the other, with its centre offset horizontally from the first by (x, y). The offset co-ordinates (x, y) are chosen at random from within the close approach area (ie. $x^2 + y^2 < (r_i + r_j)^2$). Each rod composing the first cluster is then checked against each from the second, and the point of initial impact is found. The two are then 'glued' together at this point, and the new cluster returned to the list. If the clusters miss one another (no impact at all), then they are returned to the list, and a new pair of clusters is picked.

To calculate Γ_{ij} the fall speeds of the clusters must be known. The expression (2.6) provides an explicit equation for this, however some characteristic radius r is required. Here we use the radius of gyration, defined by splitting the particle up into small elements of mass dm at position $\mathbf{r}$, and integrating over the particle volume:

$$r = \left[\frac{\int |\mathbf{r}|^2 dm}{\int dm} \right]^{\frac{1}{2}}. \tag{2.7}$$

For thin rods of length ℓ (such as our initial monomers), $r = \ell/\sqrt{12}$. After each aggregation, the radius of gyration of the new cluster may be found from the radii of the two old clusters that now compose it, by analogy with the parallel axis theorem in classical mechanics (see Goldstein 1980). If two clusters i, j with centres of mass $\mathbf{c_i}, \mathbf{c_j}$ aggregate to form a new cluster with centre $\mathbf{c_n} = (m_i \mathbf{c_i} + m_j \mathbf{c_j})/(m_i + m_j)$, then the radius of gyration of that new cluster r_n is:

$$r_n = \left[\frac{m_i(r_i^2 + |\mathbf{c_i} - \mathbf{c_n}|^2) + m_j(r_j^2 + |\mathbf{c_j} - \mathbf{c_n}|^2)}{m_i + m_j} \right]^{\frac{1}{2}}. \tag{2.8}$$

By comparison, the radii used to calculate the collision cross sections (2.1) are constructed so as to entirely enclose the clusters. This ensures that all possible close approaches may be sampled. Clusters are then picked according to the rate of close approach and tracked along a possible trajectory as described in section 2.1.1, and are either stuck together at the point of contact if a collision occurs, or returned to the list of clusters if not.

18
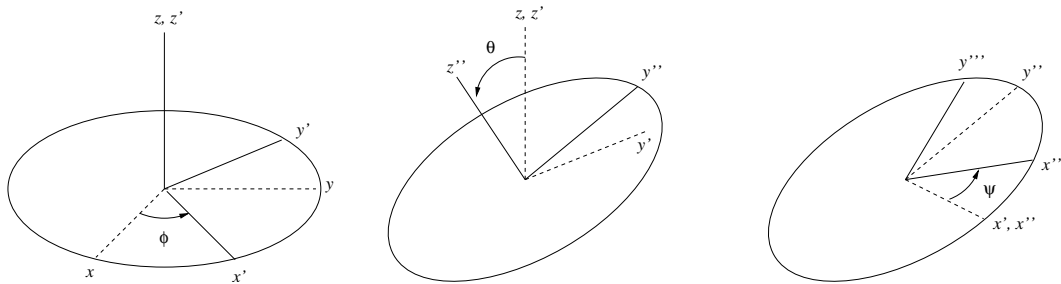
Figure 2.3: Illustration showing how the clusters are reorientated by rotation through the three Euler angles (ϕ, θ, ψ).

The orientation of the clusters is randomised between collisions, but is assumed not to change during one. Once a pair of clusters have aggregated, the newly formed cluster is rotated through the three Euler angles (ϕ, θ, ψ) as illustrated in figure 2.3. The (orthogonal) co-ordinate axes defining the orientation of the cluster (x, y, z) are rotated around the z axis by angle ϕ yielding the new set of axes (x', y', z'). Similarly, further rotations are performed around the x' axis (angle θ) and z'' axes (angle ψ) to yield the final orientation (x''', y''', z'''). To ensure that all possible orientations of the new cluster are equally probable, the angle ϕ is picked with uniform probability in the interval $[0, 2\pi]$; for the second rotation a value of $\cos\theta$ is picked with uniform probability in the range $[-1, 1]$ and θ obtained by taking the inverse cosine; the final rotation ψ is chosen randomly between $[0, 2\pi]$. How closely this scheme matches what happens to real snowflakes in a cloud is discussed at the end of this chapter.

2.3 Results

In this section we present results obtained from the computer simulations detailed above. Figure 2.4 shows sample clusters from such simulations, in this case using hexagonal columns for the pristine particles. All of the clusters shown appear to be quite different, but in this section we show that they have features which are (statistically) the same. These universal features are a result of the physics of the aggregation alone, and not of the distribution of size and shape of the monomer

19
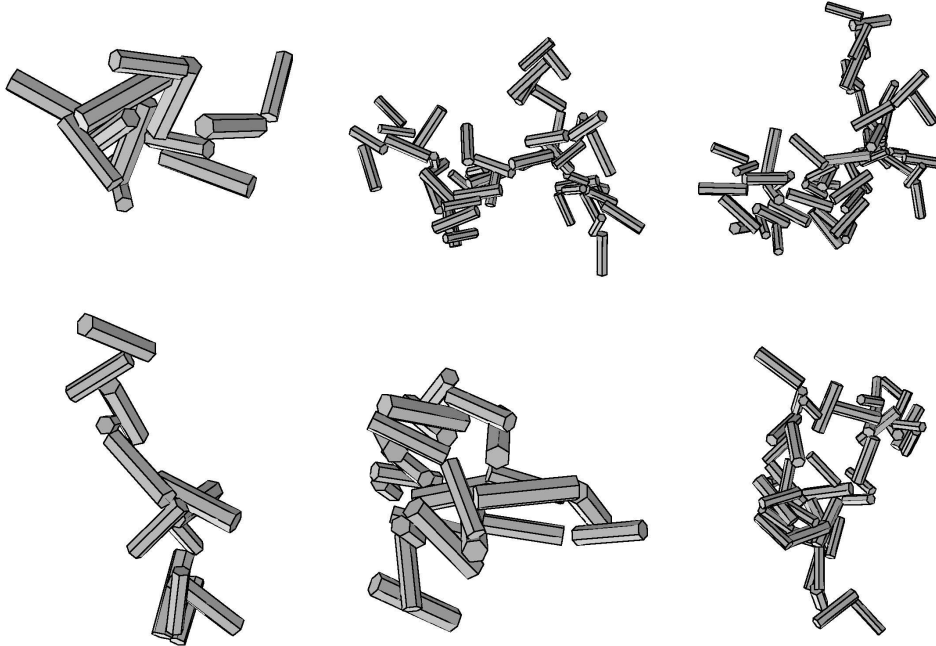
Figure 2.4: Sample aggregates of various sizes from our computer simulations. The pristine particles were hexagonal columns, with an aspect ratio of 1/8.

particles which make up the aggregates.

2.3.1 Fractal dimension

We anticipate that the clusters produced by the model will be fractal in their geometry, with mass and radius in a power law relationship $m \sim r^{d_f}$. A log plot of the average radius of gyration as a function of cluster mass for all the clusters produced over the course of the simulation is shown in figure 2.5. Shown alongside is the logarithmic derivative of that plot, showing the inverse of the local slope as a function of mass, which may be interpreted as the fractal dimension d_f. From this graph it seems that the fractal dimension approaches an asymptotic value at large cluster sizes - in the case shown ($\alpha = 0.55$) we estimate this to be $d_f = 2.2 \pm 0.1$. The asymptotic value of d_f is found to vary with the hydrodynamic exponent α, and
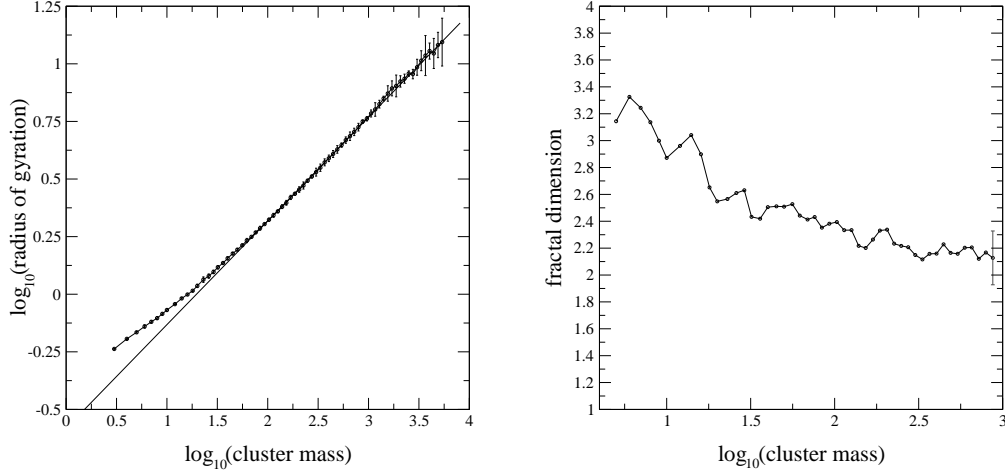
Figure 2.5: Left hand panel shows a log plot of radius of gyration as a function of cluster mass for $\alpha = 0.55$, averaged over four runs of 250,000 initial rods. Solid line indicates the theoretical prediction for the fractal dimension. The right hand panel shows the inferred fractal dimension as a function of cluster mass. Error bars are one standard deviation. Data points with $\sigma > 0.3$ have not been plotted.

this dependence is illustrated in figure 2.6 for the range $0 \le \alpha \le \frac{2}{3}$. For the physical range ($\frac{1}{2} \le \alpha \le \frac{2}{3}$) the fractal dimension increases with α from relatively open structures ($d_f \simeq 2$) for purely inertial flow, to compact clusters ($d_f = 3$) at $\alpha = \frac{2}{3}$. For $\alpha < \frac{1}{2}$ on the other hand, we find that the fractal dimension is independent of α with $d_f \simeq 2$. Note that the assumption $d_f \ge 2$, which is required to support the assumed scaling of the fall speeds in section 2.1, is satisfied in both cases.

For $\alpha > \frac{2}{3}$ (which includes the Stokes regime, $\alpha = 1$), an extrapolation of the results shown leads us to anticipate a fractal dimension of 3 (since d_f cannot increase beyond this in three-dimensional space). However, theoretical considerations (see chapter three) show that the collision kernel associated with $\alpha > \frac{2}{3}$ is somewhat pathological in its nature, and as such we have not attempted to make simulations in this regime. This is discussed further in the next chapter.

21
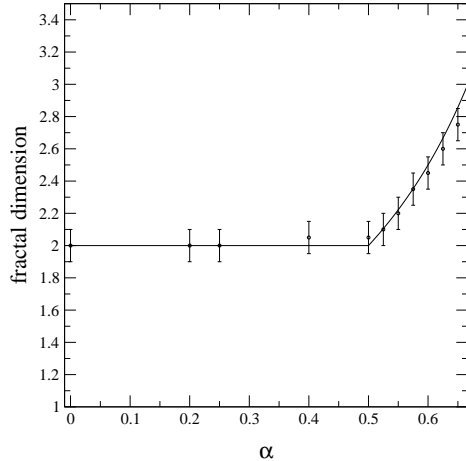
Figure 2.6: Variation of the fractal dimension as a function of the hydrodynamic parameter α. Circles are simulation data, solid line indicates theoretical prediction (see chapter three).

2.3.2 Cluster mass distribution

In this section it is demonstrated that the bin-width normalised cluster mass distribution $n(m, t)$ scales 'dynamically':

$$n(m, t) = s(t)^{-\xi} \, \phi \left[\frac{m}{s(t)} \right]. \tag{2.9}$$

where $s(t)$ is a characteristic cluster size, and ϕ is a function of the dimensionless ratio (m/s). The value of the (positive) constant ξ reflects the moment of the distribution which is conserved during the aggregation: in our simulations the total mass of the system (the first moment of the mass distribution) remains constant, and we require $\xi = 2$. Note that ϕ has the units of number concentration $[\text{cm}^{-3}]$. The essence of equation 2.9 is that the distribution at a given time t is described by an underlying distribution shape ϕ, rescaled as a function of the average cluster size $s(t)$ which characterises how far the aggregation has proceeded.

Some care is needed in constructing the characteristic cluster size s. In figure 2.7 we show a snapshot of the cluster size distribution for $\alpha = \frac{1}{2}$. At small cluster sizes the distribution is observed to take a power law form $n(m) \sim m^{-1.6}$. This power law behaviour is found for $\frac{1}{2} \leq \alpha < \frac{2}{3}$, and always has an exponent of around

22
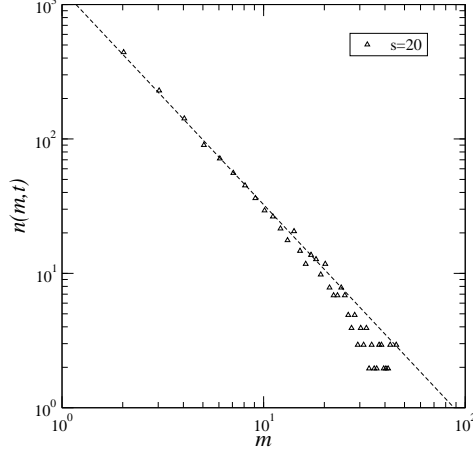
Figure 2.7: Snapshot cluster size distribution $n(m,t)$ as a function of cluster mass for $\alpha = \frac{1}{2}$, $s(t) = \sum m^2 / \sum m = 20$. At small sizes, the distribution is well described by a power law decay $n(m) \sim m^{-1.6}$.

1.6. Given the proposed dynamical scaling form (2.9), we expect that ϕ also takes a power law form $\phi(x) \sim x^{-\tau}$ with $\tau \simeq 1.6$, for small x. This has significant implications for the scaling of the moments of the size distribution M_k:

$$M_k(t) = \int_{m=1}^{m=\infty} n(m,t) m^k \mathrm{d}m \tag{2.10}$$

$$= s^{-1+k} \int_{x=1/s}^{x=\infty} \phi(x) x^k \mathrm{d}x \tag{2.11}$$

using equation (2.9). Given the anticipated divergence at the small end of the distribution, this may be rewritten as:

$$M_k \simeq s^{-1+k} \left[C \int_{x=1/s}^{x=x_c} x^{-\tau+k} \mathrm{d}x + \int_{x=x_c}^{x=\infty} \phi(x) x^k \mathrm{d}x \right]. \tag{2.12}$$

where C is a constant. For $k < \tau - 1$ the first integral diverges at large s, and the moment is dominated by the monomer population $M_k \sim s^{\tau-2}$. For $k > \tau - 1$ however, both integrals converge as $s \to \infty$, and the ratio $M_{k+1}/M_k \sim s$. Since we have measured $\tau \simeq 1.6$, we choose $s = M_2/M_1$ (ie. the weight-average cluster mass), since this is the lowest ratio of integer moments that scales correctly. This choice also imposes the normalisation $p_2/p_1 = 1$ where $p_k = \int_0^\infty \phi(x) x^k \mathrm{d}x$.

Using this choice for s, our simulation data conform well to the expected scaling. Size distribution snapshots from different stages of the aggregation were

23
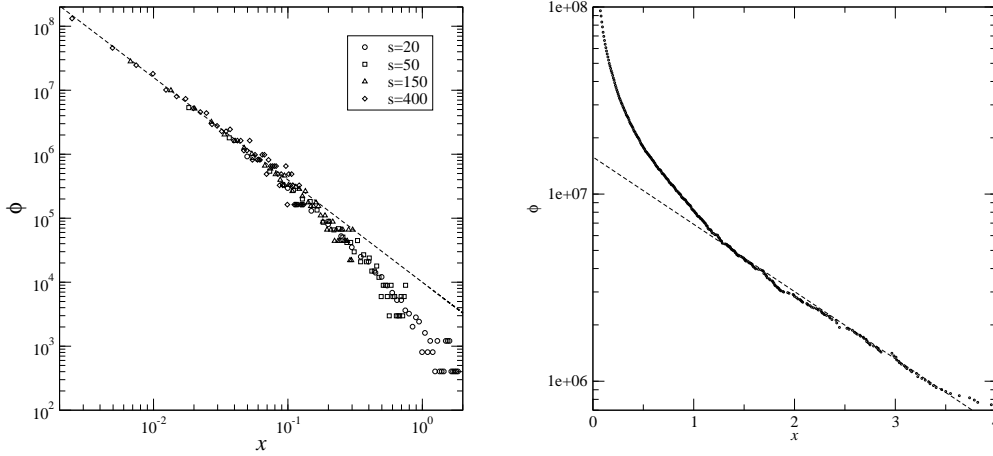
Figure 2.8: Scaling of the cluster mass distribution. The left panel shows how the rescaled cluster size distribution $\phi = s(t)^2 n_m(t)$ converges to a universal function of rescaled cluster size $x = m/s(t)$, where the data are overlayed for different values of the weight average cluster size, $s(t) = 20, 50, 150, 400$. The scales are logarithmic and a least squared fit $\phi(x) \sim x^{-1.6}$ for $x \leq 10^{-1}$ is shown by the dashed line. In the right hand panel $\int_x^\infty \phi(x')dx'$ is shown on a semi-log plot, illustrating the exponential tail (dashed line is intended to guide the eye). Both simulations began with 250,000 rods, and used $\alpha = 0.55$ in the sedimentation law.

rescaled using equation 2.9 so as to collapse the data onto the curve $\phi(x)$: this is shown in figure 2.8. The data collapse is excellent, offering strong evidence to support the dynamical scaling hypothesis.

The shape of the rescaled distribution $\phi(x)$ was studied. At small x we have already noted that the distribution is well described by an algebraic decay of the form $\phi(x) \sim x^{-\tau}$ for $\frac{1}{2} \leq \alpha < \frac{2}{3}$, as illustrated in the left hand panel of figure 2.8. The exponent τ is found to be $\simeq 1.6 \pm 0.1$ at $\alpha = \frac{1}{2}$, rising slightly to around $\tau \simeq 1.7 \pm 0.1$ at the top end of the range. For the (non-physical) regime $\alpha < \frac{1}{2}$ on the other hand, the distribution is observed to be peaked at small sizes, with a similar power law form beyond that.

In all cases the distribution is dominated by an exponential cut-off at large x: this is illustrated in the right hand panel of figure 2.8 where we show a cumulative (from the large end) plot $\int_x^\infty \phi(x')dx'$ as a function of x. This semi-log plot shows a good fit to a straight line for large x indicating an exponential cut-off. As $x \to 1$ from above, a super-exponential shape is observed as the distribution crosses over
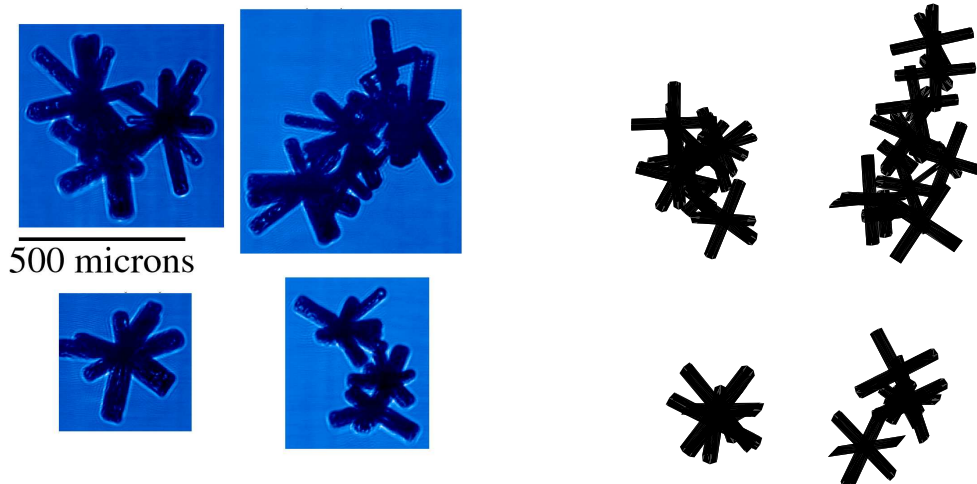
Figure 2.9: (a) Ice crystal aggregates images obtained from an aircraft flight through cirrus cloud, at temperatures from $-44°$C to $-47°$C ($\sim$9 km altitude), using a cloud particle imager (CPI, SPEC Inc., USA). The pictures shown are aggregates of rosette ice crystal types. (b) Aggregates as simulated by our computer model which assumed rigid joining when clusters collide under differential sedimentation.

to the small-x power law regime.

2.4 Comparison with experimental data

The results of our simulations are now compared to experimental data on the geometry and size distribution of snowflakes. Data from Locatelli and Hobbs (1974) show that aggregates typically fall at speeds of around 1ms^{-1}. For small aggregates ($r = 750\mu$m) this gives Re $\simeq 50$, whereas the largest aggregates ($r = 7.5$mm) have Re $\simeq 500$. These values are large enough that it seems reasonable to assume that the flow is close to the inertial regime, and the results presented in this section are those from simulations with the hydrodynamic parameter $\alpha = \frac{1}{2}$.

Aircraft flights through ice clouds have allowed researchers to collect large samples of ice particle images. In figure 2.9 aggregates of bullet-rosette crystal types imaged during a flight through a cirrus cloud are shown. These projected images allow one to study the shape and size distribution of snowflakes, and in this case

to compare the results with theoretical expectations. Shown alongside the cloud particle images in figure 2.9 are sample aggregates from our computer simulations, where the primary particles were taken to be simple three dimensional cross shapes.

Our simulated aggregates were found to obey a fractal scaling $m \sim r^{d_f}$ with $d_f = 2.05 \pm 0.1$ irrespective of the shape of the monomer particles composing them, and in chapter three we detail theoretical arguments leading to $d_f = 2$. A similar power law scaling between snowflake mass and linear span measured from experimental data has been reported by a number of authors. Heymsfield et al (2002) inferred particle mass and maximum dimension from cloud particle images of bullet-rosette aggregates such as figure 2.9, and fitted a power-law to their results. Their fitted curve corresponds to a fractal dimension of $d_f = 2.04$; in the same paper they also report observations of aggregates of side-plane type crystals, leading to $d_f = 2.08$. A study by Mitchell (1996) presents a value of $d_f = 2.1$ for aggregates of side-planes, columns and bullets. Locatelli and Hobbs (1974) report observations from a ground based instrument on aggregates of plates, side-planes, bullets and columns, leading to $d_f = 1.9$. The results of our simulations then are in close agreement with experimental data on the mass-span scaling of real ice aggregates. Data on snowflake fall speeds also provides some support for our value of d_f: since $v \sim m^{\alpha}/r$ which scales as $m^{1/2-1/d_f}$ in an inertial flow, our prediction is that the average fall speed of the snowflakes should asymptote to a roughly constant value with increasing size: this is consistent with a recent study by Barthazy and Schefold (2004) who found their data on fall speed as function of diameter was best described by a curve of the form $v \sim (1 - e^{-AD})$, where A is a constant.

Another way in which the geometry of snowflakes may be characterised is through their aspect ratio. Korolev and Isaac (2003) used images of cloud particles collected during a flight through ice clouds over Canada and the USA. They measured the maximum span of the projected images L_{max}, along with the maximum span in the direction perpendicular to that longest axis L_{perp}. The ratio of these measurements L_{perp}/L_{max} is shown in figure 2.10 as a function of L_{max}. The same ratio was calculated for random projections of our simulation clusters, and
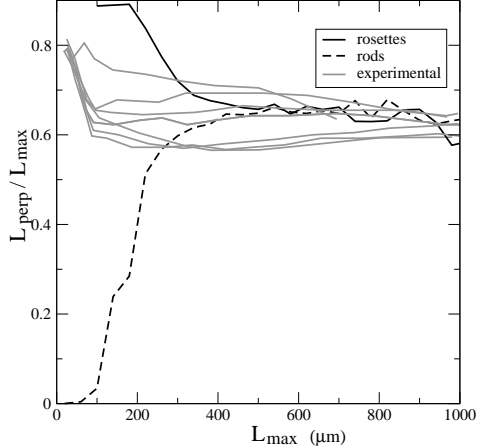
Figure 2.10: Mean aspect ratio for projected ice aggregate images, where the aspect ratio is measured as the longest span L_{max} divided into the span perpendicular to the longest L_{perp}. Grey lines show cloud data of Korolev and Isaac (2003) plotted against longest span in microns for a range of temperatures between $0°C$ and $-40°C$. Black lines show simulation data plotted against longest span in arbitrarily scaled units, where the initial particles were three dimensional crosses (solid line) and simple rods (dashed).

the results for aggregates of column (thin rod) and bullet rosette (three dimensional crossed rods) pristine particles is overlaid on the figure. In both cases, our simulated aggregates quickly asymptote to a ratio of about 0.65 ± 0.05 after only a few collisions; this appears to be mirrored by the experimental data, approaching a value of 0.6-0.7. This agreement is further evidence that our model has captured the essential features of the ice aggregate geometry.

We now make a final comparison with experimental data, by testing the dynamical scaling demonstrated by our simulated size distributions. Here we attempt to rescale the bin-width normalised particle span distributions $\frac{dN}{dD}$ presented in Field and Heymsfield (2003), and compare them to our own simulation data. The mass distribution $\frac{dN}{dm} = n(m, t)$ has already been shown to take the form:

$$\frac{dN}{dm} = s^{-\xi}\phi(m/s). \tag{2.13}$$

We now make use of the fractal scaling $m = aD^{d_f}$ where a is a constant, and obtain

27

a form for the distribution by particle span D:

$$\frac{\mathrm{d}N}{\mathrm{d}D} = ad_f D^{d_f-1} s^{-\xi} \phi(m/s) \qquad (2.14)$$

From this, the moments of the D-distribution $\mathcal{M}_k$ may be calculated:

$$\mathcal{M}_k \;\; = \;\; \int_{D_s}^{\infty} \frac{\mathrm{d}N}{\mathrm{d}D} D^k \mathrm{d}D \qquad (2.15)$$

$$= \;\; s^{-\xi+1+k/d_f} a^{-k/d_f} \int_{x=1/s}^{x=\infty} x^{k/d_f} \phi(x) \mathrm{d}x \qquad (2.16)$$

where D_s is the span of the smallest monomer particle. To avoid the divergence described in section 2.4, we choose moments with $k > d_f(\tau - 1)$ to construct the characteristic cluster span D_{av}. Since we measure $\tau \simeq 1.6$ and $d_f \simeq 2$, the second moment $\mathcal{M}_2$ is the lowest integer moment which is not dominated by the small size cut-off, and scales in the desired manner. We therefore choose $D_{av} = \mathcal{M}_3/\mathcal{M}_2 \sim s^{1/d_f}$. Normalising by $\mathcal{M}_2$, and using the fractal scaling, we find that the cluster span distribution may be written as:

$$\mathcal{M}_2^{-1} \frac{\mathrm{d}N}{\mathrm{d}D} = D_{av}^{-3} \psi\left(\frac{D}{D_{av}}\right). \qquad (2.17)$$

where the function ψ depends on the ratio D/D_{av} alone. Experimental particle span distributions sampled at various altitudes through an ice cloud are plotted in the left-hand panel of figure 2.11. These were then rescaled according to 2.17 so as to collapse the data onto the universal curve $\psi(D/D_{av})$ (right-hand panel). The data collapse is convincing, offering further evidence that aggregation is the dominant growth mechanism. Overlaid are cluster span distributions from our simulations rescaled in the same way. The correspondance is good, though not exact - in particular the 'bump' in the distribution at small sizes is not reproduced. We hypothesise that this feature is the result of physics not captured in our model such as hydrodynamic effects, or diffusional growth.

2.5   Conclusions and discussion

A simple model of aggregation through differential sedimentation has been constructed. The clusters produced have been shown to have a fractal geometry, with
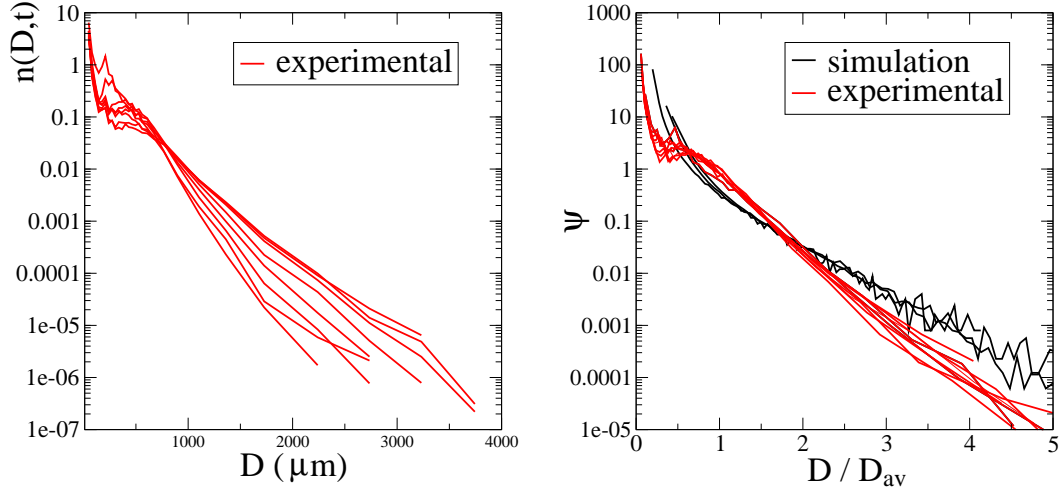
Figure 2.11: Cluster length distribution, rescaled as discussed in the text. The red lines show experimental distributions at altitudes of 9.5km ($-50°$C) to 6.6km ($-28°$C) in the cirrus cloud of Field and Heymsfield (2003) obtained during an ARM (Atmospheric Radiation Measurement program) flight (9th March 2000). Each experimental size distribution represents an in-cloud average over 15 km. Black lines show simulation data.

a fractal dimension d_f controlled by the hydrodynamic regime which the clusters are falling in. For values of the parameter $\alpha < \frac{1}{2}$, the fractal dimension is constant at $\simeq 2$; increasing α through $\frac{1}{2} \leq \alpha \leq \frac{2}{3}$ causes the d_f to increase to $\simeq 3$ at the top of that range. No simulations have been attempted for $\alpha > \frac{2}{3}$ (which includes the Stokes limit) due to theoretical issues discussed in chapter three; however we anticipate that the extrapolation $d_f = 3$ is likely to hold in such a regime.

The cluster mass distribution has been shown to conform to dynamical scaling, where a snapshot of the distribution at a given point in the system's evolution may be described in terms of an underlying distribution function ϕ, scaled by a characteristic size s. For $\alpha \geq \frac{1}{2}$ the distribution at small sizes has a power law decay $\phi \sim x^{-\tau}$ with $\tau \simeq 1.6 - 1.7$. For $\alpha < \frac{1}{2}$ by contrast, the distribution is found to be peaked at some small size, followed by a power law decay. In both regimes, the form of the distribution at large sizes is found to be dominated by an exponential cut-off.

The model has been applied to the problem of snowflake aggregation in ice

29

clouds. Measurements of typical snowflake sizes and fall speeds indicate that the flow is likely to be close to inertial, and for our comparisons we took $\alpha = \frac{1}{2}$. The fractal dimension $d_f = 2.05 \pm 0.1$ matches up well with experimental studies relating snowflake mass and linear size. The aspect ratio of our simulation clusters (0.65±0.05) also compares favourably with aircraft data from ice clouds. This agreement lends weight to the argument that some of the essential features of snowflake geometry have been captured by our model.

As a further test of the model, a scaling form for the cluster span distribution has been derived and applied to experimental data from a flight through a cirrus cloud. The data collapse from distributions sampled at different heights through the cloud is good evidence that the dynamical scaling observed in our model is mirrored in the cloud. The rescaled simulation curve is a reasonable match for the experimental one, though not perfect - in particular the 'bump' at small x remains unexplained. Suggestions for the source of this feature are physical effects not included in our model, such as diffusional growth, small clusters being swept around larger ones, wake capture, riming and cluster break up.

No details on the mechanism by which the colliding clusters adhere to one another have been included in the model. It has been assumed that any size dependence is relatively weak, and that the scaling of the collision kernel is not altered by the sticking efficiency. The close comparison between our model results and experimental data appears to support that assumption. The adhesion process itself remains a matter of considerable debate (Pruppacher and Klett 1997), with interpretations including electrical attraction, sintering and pressure melting; in addition, some authors have postulated the existence of a liquid-like layer on the crystal surfaces to account for the sticking. Understanding the adhesion mechanism of the ice crystals is a significant open question, and this is identified as an avenue for future research.

The model also includes the assumption that the clusters are orientated at random. How accurately this mirrors the situation in real ice clouds is a point of considerable uncertainty in the meteorological literature. It is known (Hallett *et al*

2002) that at fairly large Reynolds numbers, flat crystals tend to orient themselves with their plane perpendicular to the flow. Non-planar particles are thought to have a bias towards the particle falling such that its maximum projected area is at right angles to the flow; however, exactly how strong that bias is, and the distribution of canting angles for a given shape and size particle remains unclear. Electric fields in the cloud may also have an effect on the orientation of the particles (Foster and Hallett 2002). For the case of aggregation, there are also the unanswered questions of what effect the collisions themselves have on the orientation of the newly formed aggregate, and how quickly any reorientation takes place compared with the time between those collisions. Further experimental observations of snowflake orientation is needed before more sophisticated rotation schemes can be included in the model.

Chapter 3

Theory

3.1 Smoluchowski's equations

The most common theory used to describe cluster-cluster aggregation problems is that of von Smoluchowski[1] (1917). Although his equations were originally intended as a model for coagulation of colloidal particles undergoing Brownian motion, they have since been extended to describe a number of different aggregation problems. They are a set of mean-field rate equations describing the evolution of the cluster mass distribution:

$$\frac{\mathrm{d}n_k(t)}{\mathrm{d}t} = \frac{1}{2} \sum_{i+j=k} K_{ij} n_i(t) n_j(t) - n_k(t) \sum_{j=1}^{\infty} K_{kj} n_j(t) \tag{3.1}$$

where $n_k(t)$ is the number of clusters of mass k at time t (per unit volume). The kernel K_{ij} contains the physics of the problem, being a symmetric matrix, the elements of which govern the rate of aggregation between pairs of clusters expressed (only) in terms of their masses i and j. The essential content of equation 3.1 is straightforward: the rate at which the number of clusters of mass k increases (LHS) is equal to the rate at which smaller clusters stick together to produce clusters of mass k (first term, RHS), less the rate at which they themselves aggregate with others to form clusters with mass larger than k (second term, RHS).

---

[1] A more accessible reference on the origin of these equations than Smoluchowski's original paper is provided by Chandrasekhar (1943).

There are a number of assumptions implicit in equation 3.1. As in chapter two, the system is taken to be dilute so that only collisions between pairs of clusters are considered, and there is assumed to be no spatial correlation between the clusters. Also, since equation 3.1 is written in terms of cluster mass alone, all possible cluster geometries are effectively averaged over.

Exact solutions to equations 3.1 have not been found (to the author's knowledge) except for the constant ($K_{ij} = $ constant), sum ($= i + j$) and product ($= ij$) kernels. These special cases are soluble, since they allow the loss term on the RHS of equation 3.1 to be evaluated directly. This is achieved by expressing it in terms of moments of the cluster size distribution, which themselves may be calculated. The evolution of the σth moment is described by the equation:

$$\frac{\mathrm{d}M_\sigma}{\mathrm{d}t} = \frac{1}{2} \sum_{i=1}^{\infty} \sum_{j=1}^{\infty} K_{ij} n_i n_j \left\{ (i+j)^\sigma - i^\sigma - j^\sigma \right\}, \tag{3.2}$$

which is obtained by multiplying (3.1) by k^σ, summing over all k, and interchanging the order of summation[2]. In the case of the constant kernel (we take $K_{ij} = 2$ for convenience) Smoluchowski's equations become:

$$\frac{\mathrm{d}n_k(t)}{\mathrm{d}t} = \sum_{i+j=k} n_i(t) n_j(t) - 2n_k(t) M_0(t). \tag{3.3}$$

For $k = 1$, only the loss term on the RHS remains, and $\dot{n}_1 = -2n_1 M_0$. Setting $\sigma = 0$ in equation 3.2, M_0 may be evaluated: $\dot{M}_0 = -M_0^2$, and hence $M_0(t) = N/(1 + Nt)$, where N is the initial concentration at $t = 0$. Since M_0 is known, $n_1(t)$ may be calculated, and from it $n_2, n_3, n_4 \ldots$

$$n_k(t) = N \left[\frac{(Nt)^{k-1}}{(1 + Nt)^{k+1}} \right], \tag{3.4}$$

for monodisperse initial conditions $n_k(t = 0) = N\delta_{1,k}$. A similar methodology may be applied in the case of the sum and product kernels cited above, although the analysis required is somewhat more involved (see Drake 1972 and Ziff 1984).

---

[2]this is acceptable if n_k falls off quickly enough at large k that all of the moments M_σ are finite, which is certainly satisfied for kernels which are non-gelling (see section 3.2).

3.2 Van Dongen and Ernst's analysis

Although exact solutions of the Smoluchowski equations are difficult to achieve except in certain very specific cases of the coagulation kernel, some information about the large mass, long time asymptotics may still be obtained. Van Dongen and Ernst (1985) have characterised the aggregation kernel in terms of three characteristic exponents, defined through the following scaling relationships:

$$K_{ai\ aj} = a^\lambda K_{ij} \tag{3.5}$$

$$K_{i \ll j} \sim i^\mu j^\nu \tag{3.6}$$

The homogeneity exponent λ describes how much faster the aggregation rate is between larger clusters than between smaller ones, and governs the growth rate of the average cluster size $s(t)$. Depending on its value, the system may be classified as gelling (where an infinite cluster is formed in a finite time - this corresponds to $\lambda > 1$), or non-gelling ($\lambda \leq 1$). The exponents μ and ν characterise the aggregation rate between clusters of disparate sizes, and for non-gelling kernels, μ controls the qualitative form of the cluster size distribution (see below, and figure 3.1). Note that $\mu + \nu = \lambda$.

In what follows, only kernels with $\lambda \leq 1$ will be considered, since this is the case relevant to the aggregation model introduced in chapter two. Van Dongen and Ernst (1985) have shown that Smoluchowski's equations admit solutions of the form:

$$n_k(t) = s(t)^{-2} \phi[k/s(t)] \tag{3.7}$$

(which is the dynamical scaling ansatz introduced in chapter two). Substituting this into (3.1) then,

$$-s^{-3} \frac{ds}{dt} \left[x \frac{d\phi(x)}{dx} + 2\phi(x) \right] = s^{-4} \left[\frac{1}{2} \sum_{i+j=k} K_{ij} \phi(i/s) \phi(j/s) \right.$$
$$\left. - \phi(x) \sum_{i=1}^{\infty} K_{ki} \phi(i/s) \right] \tag{3.8}$$

where $x = k/s$. If we now apply the scaling relation (3.5), the differential equation can be split into two: a time dependent part describing the growth of the average

cluster size $s(t)$, and a stationary part describing the shape of the underlying cluster size distribution $\phi(x)$. Taking s to be large, and replacing the sums with integrals:

$$\frac{\mathrm{d}s(t)}{\mathrm{d}t} = ws(t)^\lambda \tag{3.9}$$

$$
\begin{aligned}
-w\left[x\frac{\mathrm{d}\phi(x)}{\mathrm{d}x} + 2\phi(x)\right] &= \lim_{\epsilon \to 0}\left[\frac{1}{2}\int_{\epsilon x}^{(1-\epsilon)x}\mathrm{d}y\,K(y, x-y)\phi(y)\phi(x-y)\right.\\
&\quad - \left.\phi(x)\int_{\epsilon x}^{\infty}\mathrm{d}y\,K(x,y)\phi(y)\right]
\end{aligned}
\tag{3.10}
$$

where w is the separation constant. The limits of integration in equation 3.10 are not explicitly set to $\epsilon = 0$, since for $\mu \geq 0$, each integral on the RHS (in isolation) diverges, whereas their sum does not (Van Dongen and Ernst 1985).

The separation constant w is related to the moments of the rescaled distribution $p_\sigma = \int_0^\infty x^\sigma \phi(x)\mathrm{d}x$. Substituting the scaling ansatz into the moment equation (3.2) gives:

$$(\sigma - 1)p_\sigma w = \frac{1}{2}\int_0^\infty \mathrm{d}x \int_0^\infty \mathrm{d}y\,K(x,y)\phi(x)\phi(y)\left\{(x+y)^\sigma - x^\sigma - y^\sigma\right\}. \tag{3.11}$$

It was noted in chapter two that our choice for $s(t) = M_2/M_1$ fixes the ratio $p_2/p_1 = 1$, while p_1 is simply equal to the total mass (per unit volume) of the system: $p_1 = M_1$. The constant w therefore also depends on the overall density of the system, and on the detailed form of the kernel K_{ij}, through equation 3.11.

The solution of equation 3.9 for the growth of the average cluster size s as a function of time at large t is straightforward:

$$s(t) \quad \sim \quad (wt)^{1/(1-\lambda)} \text{ for } \lambda < 1 \tag{3.12}$$

$$\sim \quad \mathrm{e}^{wt} \text{ for } \lambda = 1. \tag{3.13}$$

Intuitively this is sensible, since $s(t)$ grows more quickly with larger values of the homogeneity exponent λ (which characterises how much more likely collisions are between large clusters than between small ones) and for systems where the overall density of clusters is larger (and therefore more collisions occur per unit time), through the separation constant w.

The form of the rescaled distribution $\phi(x)$ is dependent on the details of the kernel, through solution of equation 3.10. As in the last section, this has not been achieved for a general K_{ij}, but only for the special cases of the constant and sum kernel[3]. The constant kernel $K_{ij} = 2$ gives:

$$\left\{ \begin{array}{l} s = M_1 t \\ \phi = M_1 \exp(-x) \end{array} \right\} \tag{3.14}$$

which is equivalent to the exact solution (3.4) in the limits $k, s(t) \to \infty$, k/s finite, whilst the sum kernel $K_{ij} = i + j$ gives:

$$\left\{ \begin{array}{l} s = \exp(2M_1 t) \\ \phi = M_1 \pi^{-1/2} x^{-3/2} \exp(-x) \end{array} \right\}. \tag{3.15}$$

Although these are the only directly soluble cases, some information about the asymptotics for $x \ll 1$ and $x \gg 1$ may be obtained for a general K_{ij}. Van Dongen and Ernst (1985) classify the small x behaviour through the exponent μ, defined in the scaling relation 3.6. If $\mu \geq 0$, the distribution takes a power law form $\phi(x \ll 1) \sim x^{-\tau}$. This classification may be split into two further cases. For $\mu > 0$, where the aggregation is dominated by collisions between pairs of large clusters, the exponent τ depends only on λ since this governs how much more favourable collisions between big clusters are than between small ones, and $\tau = 1 + \lambda$. In the marginal case $\mu = 0$ however, neither big-big nor big-little events are dominant, and τ is sensitive to the detailed form of the kernel, not merely the scaling (3.5). Van Dongen and Ernst show $\tau = 2 - p_\lambda/w$, and as a result conclude that its value may only be determined after the full solution to $\phi(x)$ has been obtained; a more recent study by Cueille and Sire (1997) has outlined methods for obtaining analytical bounds and numerical estimates for τ without knowing the complete functional form of $\phi(x)$, when certain conditions on the form of K_{ij} are satisfied. In the final case ($\mu < 0$), the small x behaviour is dominated by the loss term in equation 3.10, and a 'bell-shaped' distribution is obtained: ϕ vanishes exponentially as $x \to 0$, with a peak at some small size x_m and a power law decay for $x_m \ll x \ll 1$. This

---

[3]The third soluble case is the product kernel. Since $\lambda = 2$ this is a gelling kernel, and a different scaling ansatz $n_k = s^{-\tau} \phi(k/s)$, with $\tau = \frac{1}{2}(3+\lambda)$ must be used - see Van Dongen and Ernst (1985).
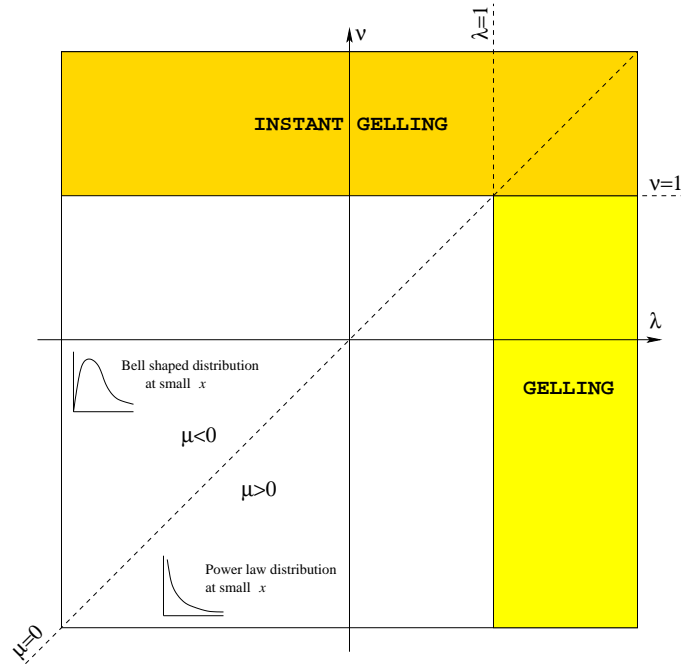
Figure 3.1: Classification of the aggregation behaviour in terms of the characteristic exponents μ, ν and $\lambda = \mu + \nu$, where $K_{i \ll j} \sim i^\mu j^\nu$.

classification of the aggregation kernel in terms of the characteristic exponents is illustrated in the 'phase diagram', figure 3.1. For $x \gg 1$, Van Dongen (1987b) has shown that the cluster size distribution has an exponential tail $\phi(x \gg 1) \sim \mathrm{e}^{-\delta x}$ (with some positive constant δ), for all non-gelling kernels. This is discussed in more detail in section 3.5.

In addition to delineating the $\mu < 0$ and $\mu \geq 0$ cases, figure 3.1 also contains a region marked 'gelling' which corresponds to $\lambda > 1$ (as previously discussed), and another marked 'instant gelling', corresponding to $\nu > 1$. In the latter case, Van Dongen (1987a) has shown that Smoluchowski's equations predict the formation of an infinite cluster instantly. In a finite system, this clearly cannot occur; however the dynamics become completely dominated by events where a large cluster aggregates with much smaller ones. In such a regime, the mass of the large cluster grows as $\mathrm{d}k/\mathrm{d}t \simeq \int_0^\infty K_{ki} n_i i \,\mathrm{d}i \sim k^\nu$, and as a result a few clusters become very large, very quickly. Recent numerical work by Lee (2000) has indicated that in such a case, runaway growth (gelation) sets in at a critical time t_c, the value of which decreases

slowly towards $t_c \to 0$ as the initial number of clusters per unit volume is increased.

The discontinuity between the extreme runaway growth of $\nu > 1$, and the controlled, non-gelling behaviour of $\nu \leq 1$, $\lambda \leq 1$ is the basis of the argument put forward in section 3.4 for how the geometry and the dynamics feed back on one another to stabilise the fractal dimension and growth exponents.

3.3 Application to differential sedimentation

In the model presented in chapter two, collisions were sampled by picking pairs of clusters with a probability proportional to a rate of close approach $\Gamma_{12} = \pi(r_1 + r_2)^2 |v_1 - v_2|$, after which they were tracked along one of those possible close approach trajectories, to see if a collision actually took place. In the theoretical analysis that follows, we make the simplifying assumption that all (or a fixed fraction) of the close approaches lead to collisions. This seems reasonable provided that the fractal dimension of the clusters is at least two (as suggested by our simulations), since then their projection should fill the plane uniformly. Using the explicit form assumed for the fall speeds ($v \sim m^\alpha/r$) and the observed fractal scaling ($m \sim r^{d_f}$), the collision rate may be rewritten in terms of the cluster masses alone:

$$K_{ij} \sim (i^{1/d_f} + j^{1/d_f})^2 \left| i^{\alpha - 1/d_f} - j^{\alpha - 1/d_f} \right| \tag{3.16}$$

which, in terms of the Van Dongen & Ernst analysis in the previous section, yields the characteristic exponents:

$$\mu = \min(0, \alpha - d_f^{-1}) \tag{3.17}$$

$$\nu = \max(\alpha + d_f^{-1}, 2d_f^{-1}) \tag{3.18}$$

$$\lambda = \alpha + d_f^{-1}. \tag{3.19}$$

These exponents then are influenced both by the hydrodynamic regime governing the motion of the clusters (through α) and their geometry (through the fractal dimension).

3.4 The self-organisation of the system

In this section, an argument is put forward for how the geometry of the clusters (characterised by d_f) and the dynamics of their aggregation (characterised by μ, ν and λ) feed back on one another to stabilise all four exponents at predictable values. In particular, the identification of the growth exponent ν, and its dependence on the fractal dimension d_f is crucial to this argument.

We first consider the case where $d_f < \max\{1/(1-\alpha), 2\}$, and as a result the exponent ν is larger than unity. We therefore expect runaway growth, with a few large clusters growing very quickly by 'mopping up' lots of much smaller ones. In such a regime the intuitive expectation is that the small clusters will penetrate relatively deeply into the large cluster, making the structure more compact. Ball and Witten (1984) studied the case of small particles moving along ballistic trajectories and impacting on a much larger cluster, and showed that the resulting aggregates are indeed compact, ie. $d_f = 3$. For $\alpha < \frac{2}{3}$ such a high fractal dimension is inconsistent with the hypothesis that $\nu > 1$. We conclude that the extreme dynamics associated with $\nu > 1$ are not sustainable in this case, and hence $d_f \geq \max\{1/(1-\alpha), 2\}$.

Because of the runaway growth associated with $\nu > 1$, the size distribution becomes very polydisperse: the Smoluchowski equations predict one infinite cluster mopping up all remaining finite size clusters in a vanishingly small time. In finite systems, numerical work has indicated an algebraic tail $n_k \sim k^{-\nu}$ (Lee 2000). The distribution for $\nu < 1$, $\lambda < 1$ (corresponding to $d_f < \max\{1/(1-\alpha), 2\}$) is relatively monodisperse by comparison (since for non-gelling systems n_k is exponentially bounded at large cluster sizes), and as a result collisions between clusters of a similar size are much more likely. The result of such a scenario is more open structures, with low fractal dimension. This in turn acts as a feedback mechanism to increase ν towards unity. The author suggests that (at least over some range of α) this will stabilise the system at the marginal case $\nu = 1$.

If it is accepted that $\nu \to 1$ then the fractal dimension of the clusters produced
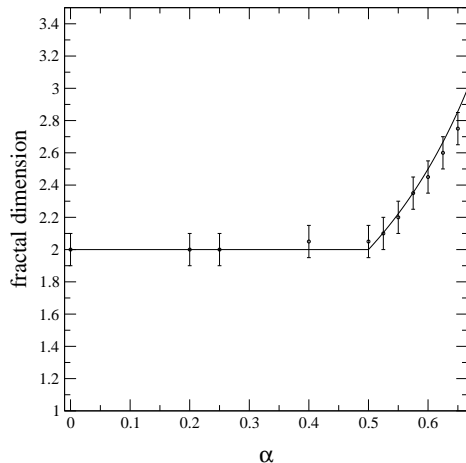
Figure 3.2: Variation of the fractal dimension as a function of the hydrodynamic parameter α. Circles are simulation data, solid line indicates theoretical prediction (note: this figure is reproduced from section 2.3).

ought to be directly predictable from equation (3.18):

$$d_f = \max\{2, 1/(1 - \alpha)\}, \quad \text{for } \alpha \leq \tfrac{2}{3}. \tag{3.20}$$

A curve showing this theoretical prediction is plotted in figure 3.2, showing excellent agreement with the superimposed simulation data for the range of α considered ($0 \leq \alpha \leq \tfrac{2}{3}$). For $\alpha > \tfrac{2}{3}$ the theoretical prediction is that $d_f = 3$ and $\nu = \alpha + \tfrac{1}{3} > 1$; however no simulations were attempted in this range, because of the extreme dynamics associated with the regime $\nu > 1$. From the extrapolation of the data in figure 3.2 though, it seems likely that the prediction ought to hold.

3.5   Shape of the cluster size distribution

In this section we consider what information about the shape of the cluster size distribution $\phi(x)$, and the universal exponents associated with it for small and large x, may be obtained for our differential sedimentation kernel. As described in section 3.2, at small cluster sizes ($x \ll 1$) the distribution can take one of two forms depending on the value of μ. Using equation 3.17 and our prediction for the fractal

dimension, we find $\mu = \min\{0, 2\alpha - 1\}$. For $\frac{1}{2} \le \alpha \le \frac{2}{3}$ then, we expect $\mu = 0$ and $\phi \sim x^{-\tau}$, with $\tau < 2$ (by mass conservation arguments). This is in agreement with our simulation results where we find a power law decay with exponent $\tau \simeq 1.6 - 1.7$. For the (non-physical) regime $\alpha < \frac{1}{2}$, we expect $\mu = 2\alpha - 1 < 0$, and the theoretical expectation is that $\phi(x)$ vanishes exponentially as $x \to 0$. To obtain a more detailed form for $\phi(x \ll 1)$ we follow the methodology of Van Dongen and Ernst (1985). We anticipate that the small size behaviour in this regime is dominated by collisions between clusters of disparate sizes, and as a result the gain term in equation 3.10 may be neglected. We therefore attempt to solve the integro-differential equation $w[x\phi'(x) + 2\phi(x)] = \phi(x)\int_0^\infty K(x,y)\phi(y)\mathrm{d}y$. For $x \ll y$, the kernel (3.16) may be approximated to $K(x,y) \simeq x^\mu y^\nu - y^\lambda$, and one obtains:

$$\phi(x) = x^{-\tau'} \exp\left[\frac{x^\mu p_\nu}{w\mu}\right] \tag{3.21}$$

where the exponent $\tau' = 2 + p_\lambda/w$. This functional form is consistent with our simulation results for $\alpha < \frac{1}{2}$, where the monomer population is almost completely depleted, but at slightly larger cluster sizes shows a peak, followed by a power-law like decay. This discontinuity in the qualitative shape of the distribution at small x is further evidence that the system selects to sit at $\nu = 1$.

At large cluster sizes ($x \gg 1$), the distribution becomes dominated by an exponential cut-off. To obtain a more precise functional form for this regime, Van Dongen (1987b) looked for solutions to the Smoluchowski equations of the form:

$$\phi = \Lambda x^{-\theta} \mathrm{e}^{-\delta x} \tag{3.22}$$

where Λ, δ and θ are constants. When $\nu < 1$, the exponent θ in (3.22) is identical to the homogeneity exponent λ. However, in section 3.4 it was shown that for our differential sedimentation kernel, the system is forced to the marginal regime $\nu = 1$. In this case, the value of θ is sensitive to the details of K_{ij}, and not simply the scaling (3.5,3.6). We follow the methodology of Van Dongen (1987b) and rewrite the kernel in the form:

$$K(i,j) = (ij)^\mu (i+j)^{1-\mu}[1 + Q(i,j)]. \tag{3.23}$$

41

For small $u = i/j$, the leading order term in Q is:

$$Q(u, 1 - u) \simeq qu^\rho + \ldots \tag{3.24}$$

with $q = 1$, $\rho = 1$ for our differential sedimentation kernel (3.16). Substituting the ansatz (3.22) into equation 3.10, dividing through by $x\phi(x)$, and dropping terms of order x^μ or smaller, the following equation is obtained:

$$
\begin{aligned}
w\delta \quad \simeq \quad & \lim_{\epsilon \to 0} \left\{ \int_{\epsilon x}^{x/2} y^\mu \phi(y) e^{\delta y} dy \right. \\
& + \int_{\epsilon x}^{x/2} \left[K(y, x - y)\phi(x - y)/(x\phi(x)) - y^\mu e^{\delta y} \right] \phi(y) dy \\
& \left. - \int_{\epsilon x}^{\infty} (y^\mu \phi(y) + \ldots) \, dy \right\}
\end{aligned}
\tag{3.25}
$$

Combining the first and third terms on the RHS, and making use of the ansatz (3.22):

$$w\delta \simeq \int_0^\infty y^\mu \phi(y) \left(e^{\delta y} - 1 \right) dy + x^{1+\mu} \phi(x) e^{\delta x} J(\theta) \tag{3.26}$$

where

$$J(\theta) = \int_0^{1/2} \left\{ K(u, 1 - u) \left[u(1 - u) \right]^{-\theta} - u^{\mu - \theta} \right\} du - \int_{1/2}^\infty u^{\mu - \theta} du, \tag{3.27}$$

and $u = y/x$. Note the integral converges only for $(1 + \mu) < \theta < (1 + \mu + \min\{1, \rho\})$, so for the physical hydrodynamic regime (corresponding to $\frac{1}{2} \le \alpha \le \frac{2}{3}$, $\mu = 0$) we expect $1 < \theta < 2$. The leading order terms of equation 3.26 ($\sim x^0$) may be equated, but the second term on the RHS ($\sim x^{1+\mu-\theta}$) has nothing to balance it, so we require $J(\theta) = 0$, which provides a (transcendental) equation for the exponent θ. In figure 3.3 the function $J(\theta)$ is plotted for our differential sedimentation kernel at various values of the hydrodynamic parameter α, using our prediction $d_f = 1/(1 - \alpha)$. Also shown are model results for two other kernels with $\nu = 1$: the sum kernel $K_{ij} = i + j$, which has one root at $\theta = 1.5$ in accordance with the exact solution (3.15), and $K_{ij} = (i^{1/2} + j^{1/2})^2$ which has three solutions: $\theta = 1.17, 1.5, 1.77$. For the differential sedimentation kernel there are four roots for $0.525 \le \alpha \le 0.65$ — these are tabulated in table 3.1. Which one of these possible values of θ represents the true exponent is unclear; the constants Λ and δ also remain unknown. For $\alpha = \frac{1}{2}$,
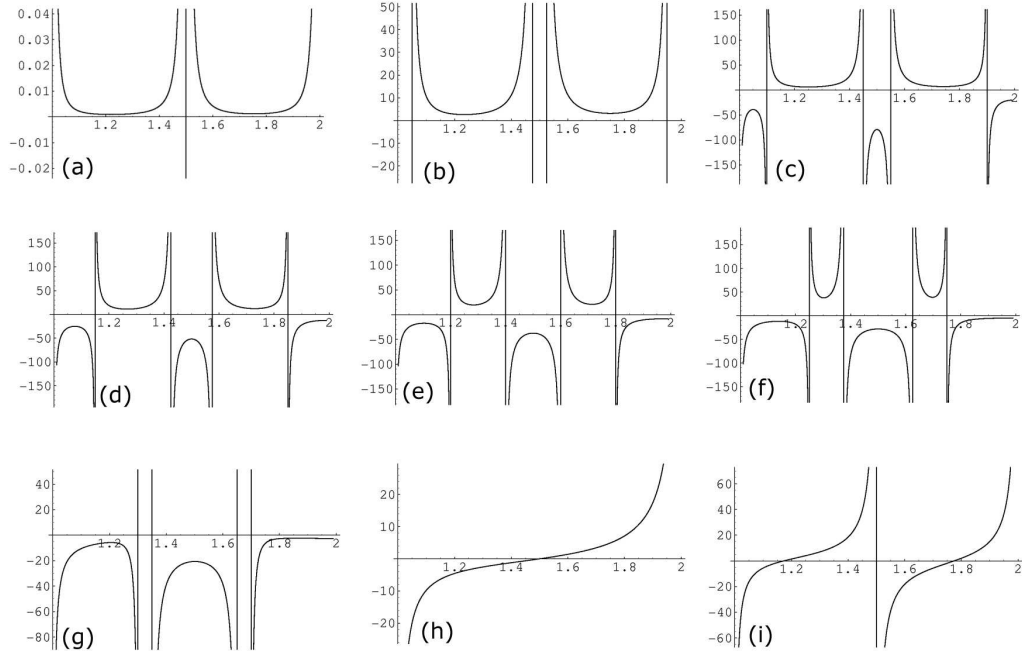
Figure 3.3: $J(\theta)$ for the differential sedimentation kernel, at different values of the hydrodynamic parameter: a) $\alpha = 0.50001$, b) 0.525, c) 0.55, d) 0.575, e) 0.6, f) 0.625, g) 0.65. Also shown are two model kernels with $\nu = 1$: h) the sum kernel $K_{ij} = i + j$ and i) $K_{ij} = (i^{1/2} + j^{1/2})^2$

$\alpha \rightarrow$	0.525	0.550	0.575	0.600	0.625	0.65
$\theta_1 \simeq$	1.05	1.10	1.15	1.20	1.25	1.30
$\theta_2 \simeq$	1.48	1.45	1.42	1.40	1.37	1.35
$\theta_3 \simeq$	1.52	1.55	1.57	1.60	1.63	1.65
$\theta_4 \simeq$	1.95	1.90	1.85	1.80	1.75	1.70

Table 3.1: the four roots of $J(\theta) = 0$ (see text) for our differential sedimentation kernel, at six different values of the hydrodynamic parameter α. All the quoted exponents have an estimated error of ± 0.01.

$d_f = 2$ the kernel K_{ij} expressed only in terms of cluster mass as per equation 3.16 is zero, since all of the cluster fall speeds are identical. In reality we only expect the *average* fractal dimension to approach two, and it is the fluctuations around this value that drive the aggregation. We are therefore unable to calculate $J(\theta)$ for this case. We have however attempted to study what happens in this limit by looking at values of α approaching it: an example is shown in figure 3.3. It appears that as $\alpha \to \frac{1}{2}$ the two outermost roots disappear, and the two inner roots converge towards a value of 1.5. We therefore expect that in the purely inertial regime $\theta = 1.5$.

3.6   Consistency with measured size distributions

In the simulations detailed in chapter two, it was found that the cluster mass distribution had an exponentially dominated cut-off at large x, consistent with the form (3.22). However, the distributions by cluster *span* also showed a roughly exponential decay at large sizes, both in our simulations, and in the experimental data (figure 2.11) over the range $D/D_{av} \simeq 1 - 5$. Given the proposed fractal scaling $m \sim D^{d_f}$ this would appear inconsistent. However, if the full form (3.22) for the distribution at large sizes is used, then the rescaled distribution takes the form:

$$\left[\frac{1}{\mathcal{M}_2}\frac{\mathrm{d}N}{\mathrm{d}D}D_{av}^3\right] \sim \left(\frac{D}{D_{av}}\right)^{-1-d_f(\theta-1)} \exp\left\{-\delta'(D/D_{av})^{d_f}\right\} \qquad (3.28)$$

where δ' is a constant. This combination of a 'squashed exponential' cut-off with a power law prefactor for the diameter distribution does in fact provide a form consistent with the approximately experimental data. For $(D/D_{av}) > 1$, but not too large, such a function can closely mimic an exponential over a significant range of (D/D_{av}), provided the constant δ' is not too big or too small (so that neither factor dominates). As an example, figure 3.4 shows a semi-log plot of $\left[\mathcal{M}_2^{-1}\frac{\mathrm{d}N}{\mathrm{d}D}D_{av}^3\right]$ for the same range of D/D_{av} as figure 2.11. We have used our predicted exponents for the inertial regime: $d_f = 2$, $\theta = 1.5$. The constant δ' remains unknown: here we show the curve for $\delta' = 0.1$, and the resulting plot very convincingly mimics an exponential distribution.
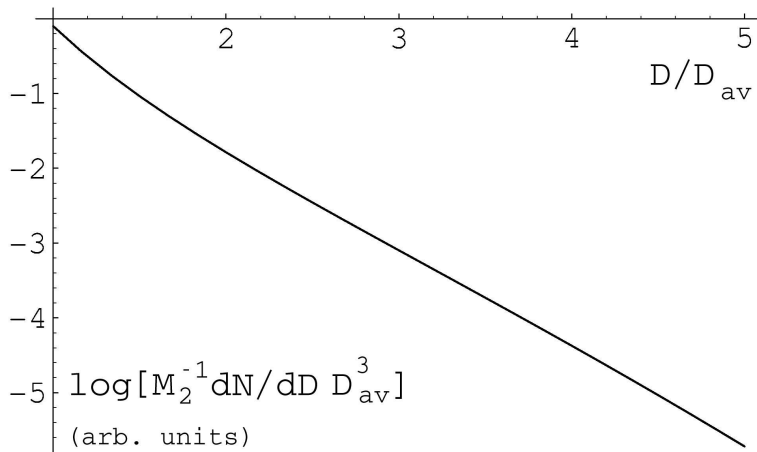
Figure 3.4: Theoretical prediction for the rescaled cluster span distribution at large sizes in an inertial flow. The value of the (unknown) parameter δ' is 0.1 (see text). The curve convincingly mimics an exponential decay for the range shown (the same range as the simulation and experimental data shown in figure 2.11).

3.7 Discussion

In this section the differential sedimentation model introduced in chapter two has been analysed in terms of the Smoluchowski equations. We have pre-averaged over all possible cluster geometries in order to express the rates of aggregation between pairs of clusters in terms of their mass alone, using the fractal scaling $m \sim r^{d_f}$. The growth has been characterised in terms of the hydrodynamic parameter α and fractal dimension d_f, through the exponents μ, ν and λ.

The system has been shown to self-organise so as to stabilise the exponent ν at unity. Above this value, the dominance of collisions between clusters of very different sizes is so great as to push d_f towards a value of 3. This in turn pulls ν back down to unity. For $\nu < 1$ the system is much more monodisperse, resulting in relatively many collisions between clusters of similar sizes, leading to more open structures with low fractal dimension, pulling ν back up. This feedback mechanism results in the system selecting to sit at $\nu = 1$, for $\alpha < \frac{2}{3}$. The fractal dimension of the clusters is then directly predictable: $d_f = \max\{1/(1-\alpha), 2\}$. This is in

excellent agreement with our simulations, and the result for inertial flow provides a good match with experimental data ($d_f = 2$).

The shape of the distribution $\phi(x)$ has been studied in the small and large x limits. For small cluster sizes, the qualitative form of $\phi(x \ll 1)$ is expected to be a power law $\sim x^{-\tau}$ for $\frac{1}{2} \leq \alpha \leq \frac{2}{3}$, whereas for $\alpha < \frac{1}{2}$, we expect ϕ to vanish exponentially as $x \to 0$, with a peak at some small size x_m, and a power law for $x_m \ll x \ll 1$. This discountinuity in the shape of the distribution around $\alpha = \frac{1}{2}$ is observed in our simulations, and provides further evidence for the proposed self organisation to $\nu = 1$.

At large cluster sizes the distribution takes the form $\phi(x) \sim x^{-\theta} e^{-\delta x}$. Possible values of the exponent θ have been found by looking for solutions to the equation $J(\theta) = 0$; however there is in general more than one root to this equation, and which value corresponds to the true value of the exponent is unclear. In the inertial limit $\alpha = \frac{1}{2}$ it appears that there is only one root at $\theta = 1.5$. The constant δ remains unknown. This predicted behaviour is found to be consistent with our simulation results and experimental data.

Chapter 4

Application to radar scattering

4.1 Introduction

In this chapter the results from the previous two chapters on the geometry and distribution of aggregate snowflakes are applied to the problem of modelling their radar scattering properties. Since the 1940s, the potential of radar to both detect clouds and to make quantitative measurements of their microphysical properties has been recognised. A transmitter generates microwave pulses which are focussed by an antenna. The snowflakes have a different dielectric constant to that of the air, and as a result scatter the incoming wave, part of which returns back to the antenna and is measured by a receiver.

The time between the transmission of the pulse and the reception of its reflection is the most basic measurement, and allows the position of the snowflakes to be fixed. In addition, the intensity of the reflected pulse may also be measured. In this chapter we attempt to relate this intensity to the microphysical properties of the cloud, such as ice water content and precipitation rate. The back scatter from our simulated aggregates is calculated using the Rayleigh-Gans approximation, and the results compared to simplified analytic expressions from the literature. The total scattering is then obtained by integrating over the size distribution, and the physical interpretation of the results is considered. In particular we study how measurements of the back scattered intensity may be related to quantities of meteorological interest,
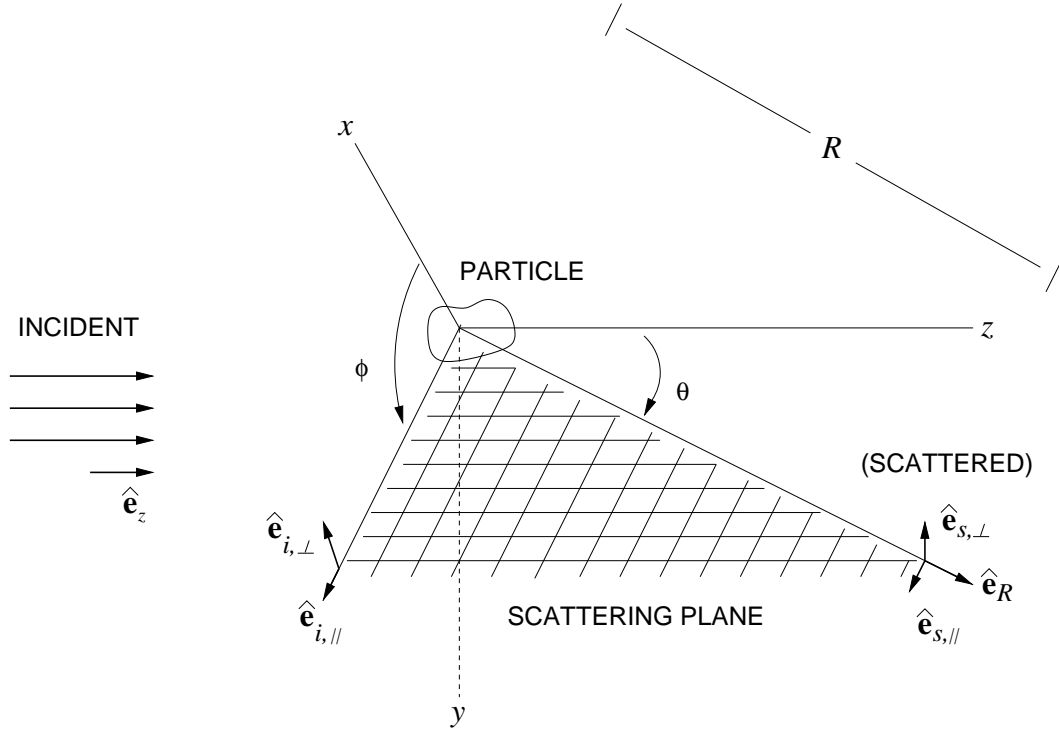
Figure 4.1: Illustration of an incident electromagnetic wave being scattered by a particle. The incident wave is travelling in the z direction; the scattered wave is measured at (R, θ, ϕ) and so the part of the scattered wave of interest is travelling in the $\widehat{\mathbf{e}}_R$ direction. The direction of polarisation of the waves is specified in terms of components perpendicular and parallel to the scattering plane (defined by $\widehat{\mathbf{e}}_z$ and $\widehat{\mathbf{e}}_R$), through the basis vectors $(\widehat{\mathbf{e}}_{i,\parallel}, \widehat{\mathbf{e}}_{i,\perp})$ and $(\widehat{\mathbf{e}}_{s,\parallel}, \widehat{\mathbf{e}}_{s,\perp})$.

such as ice water content and precipitation rate. Finally a comparison is made between our calculations for the simulated aggregates and a sphere composed of a homogeneous mixture of air and ice, which is the model commonly used in the meteorological literature (eg. Hogan and Illingworth 2000).

4.2 Scattering of electromagnetic waves

Here we introduce the problem of calculating the scattering of an incident electromagnetic wave (a radar pulse) by a particle (a snowflake), as illustrated in figure 4.1. The incident electric field is taken to be a plane wave with wavelength λ, travelling

in the z direction:

$$\mathbf{E}_i = (E_0 \mathrm{e}^{ikz - i\omega t})\widehat{\mathbf{e}}_{i,p} \tag{4.1}$$

where the basis vector $\widehat{\mathbf{e}}_{i,p}$ represents the polarisation of the wave, E_0 is its amplitude, ω its (angular) frequency, and $k = 2\pi/\lambda$. It is convenient to express the incident and scattered fields in terms of their components parallel and perpendicular to the scattering plane, so that:

$$\mathbf{E}_i = E_{i,\|}\widehat{\mathbf{e}}_{i,\|} + E_{i,\perp}\widehat{\mathbf{e}}_{i,\perp}, \quad \mathbf{E}_s = E_{s,\|}\widehat{\mathbf{e}}_{s,\|} + E_{s,\perp}\widehat{\mathbf{e}}_{s,\perp}. \tag{4.2}$$

Note that $\widehat{\mathbf{e}}_{i,\perp} \times \widehat{\mathbf{e}}_{i,\|} = \widehat{\mathbf{e}}_z$. We are interested in the 'far field' regime $R \gg \lambda$, where the scattered wave is well known (Jackson 1975, p.478) to be approximately transverse ($\widehat{\mathbf{e}}_{s,\perp} \times \widehat{\mathbf{e}}_{s,\|} = \widehat{\mathbf{e}}_R$), with an electric field of the form $|E_s| \sim \mathrm{e}^{ikR}/(-ikR)$. As a result the scattered field is usually written in the form:

$$\begin{pmatrix} E_{s,\|} \\ E_{s,\perp} \end{pmatrix} = \frac{\mathrm{e}^{ik(R-z)}}{-ikR} \begin{pmatrix} S_2 & S_3 \\ S_4 & S_1 \end{pmatrix} \begin{pmatrix} E_{i,\|} \\ E_{i,\perp} \end{pmatrix} \tag{4.3}$$

where the S_n are the elements of the 'amplitude scattering matrix', relating the scattered field to the incident one – these are the functions that we would like to calculate for our snowflakes. In principle, this could be achieved through solution of Maxwell's equations in and outside the particle:

$$\mathrm{div}\,\mathbf{E} = 0 \tag{4.4}$$

$$\mathrm{div}\,\mathbf{H} = 0 \tag{4.5}$$

$$\mathrm{curl}\,\mathbf{E} = i\omega\mu'\mathbf{H} \tag{4.6}$$

$$\mathrm{curl}\,\mathbf{H} = -i\omega\epsilon'\mathbf{E} \tag{4.7}$$

where μ' and ϵ' are the permeability and permittivity of the particle/surrounding medium[1]. In practice this has not been achieved except for a few rather idealised cases; in particular Mie[2] (1908) solved the case of an isotropic dielectric sphere

---

[1]Note that $\epsilon' = \epsilon_0\epsilon$ where ϵ_0 is the permittivity of free space, and ϵ is the relative permittivity or dielectric constant. At microwave frequencies, the dielectric constant of ice is $\epsilon \simeq 3.2$ [Warren (1984)].

[2]A more accessible reference on the Mie solution is provided by Bohren and Huffman (1983)

of radius a. He expressed the matrix elements as a set of series expansions, and the scattering for a sphere of any size may be computed to an arbitrary degree of accuracy simply by calculating more terms in the series. Importantly, for spheres much smaller than the wavelength ($ka \to 0$) the elements reduce to:

$$S_1 = -ik^3 \left| \frac{\epsilon - 1}{\epsilon + 2} \right| a^3 \qquad (4.8)$$

$$S_2 = -ik^3 \left| \frac{\epsilon - 1}{\epsilon + 2} \right| a^3 \cos\theta \qquad (4.9)$$

and $S_3 = S_4 = 0$. This is the Rayleigh limit, and yields the well known $\sim a^6/\lambda^4$ dependence for the scattered intensity $|\mathbf{E}_s|^2$.

In general we would like a way of relating the incident and scattered intensities: this is provided by the differential scattering cross section $\frac{d\sigma}{d\Omega}(\theta, \phi)$ which is the amount of power scattered into the solid angle $d\Omega$ about (θ, ϕ), and is simply:

$$\frac{d\sigma}{d\Omega}(\theta, \phi) = \frac{|\mathbf{E}_s|^2}{|\mathbf{E}_i|^2} R^2. \qquad (4.10)$$

Here we consider the case of unpolarised incident radiation, and so only the average of $\frac{d\sigma}{d\Omega}$ over all polarisations (ie. over ϕ) is relevant. For example in the case of the Rayleigh sphere the differential cross section is:

$$\frac{d\sigma}{d\Omega} = \frac{k^4 a^6}{2} \left| \frac{\epsilon - 1}{\epsilon + 2} \right|^2 (1 + \cos^2\theta). \qquad (4.11)$$

For our application, we are interested in how much of the transmitted radar pulse is reflected back towards the antenna, ie. the back scatter ($\theta = \pi$). The 'radar cross section' of a single cloud particle is defined to be:

$$\sigma_r = 4\pi \left. \frac{d\sigma}{d\Omega} \right|_{\theta = \pi} \qquad (4.12)$$

and the *total* radar cross section (or 'reflectivity') is then simply the sum of the cross sections of the individual particles per unit volume of cloud $\eta = \sum \sigma_r$ (since the cloud is relatively dilute, multiple scattering between the individual cloud particles is neglected). It is this quantity that is measured in experiments, and the purpose of the remainder of this chapter is firstly to try and calculate the radar cross section of an individual snowflake, and then to obtain the reflectivity for a distribution of snowflakes. These results are then applied to the problem of using radar data to infer the microphysical properties of ice clouds.

4.3 The Rayleigh-Gans theory

In the previous section the amplitude scattering matrix elements for a sphere much smaller than the wavelength were given. Ice particles in clouds however are not spherical (a glance at figure 2.9 will assure the reader of this), and many of them are of a size comparable to millimetric radar wavelengths. To estimate the scattering from snowflakes then, we must use a more sophisticated method, and here we employ the Rayleigh-Gans theory[3]. The essence of this approximation is that the particle is treated as being constructed from a number of small volume elements, where each element behaves as a Rayleigh scatterer. We ignore any interactions between the elements (each one sees only the applied incident wave), and calculate the total scattered field by summing up the contributions from each of them. From this, the radar cross section of the complete particle is obtained.

In the case of our aggregate snowflakes, we assume that the pristine particles that compose them are sufficiently small compared to the radar wavelength that they may be considered to be in the Rayleigh regime. This seems reasonable, since pristine ice crystals are rarely more than a few hundred μm, whereas radar wavelengths are usually at least a few millimetres, if not longer. Given this assumption, we proceed to calculate the radar cross section for the complete aggregate via the Rayleigh-Gans theory. In chapter two we found that the geometry of our aggregates is universal (in a statistical sense), and in what follows we show that the effect of particle shape on the scattering may be described in terms of a single dimensionless function (the form factor - see below). We have calculated this function for our synthetic snowflakes, and in the next section we compare it to analytical results from the physics literature.

The starting point for the Rayleigh-Gans approximation is the scattering matrix elements for the Rayleigh sphere (4.8, 4.9). Dividing these by the volume $v = \frac{4}{3}\pi a^3$ gives the quantities:

$$s_1 \quad = \quad -\frac{3ik^2}{4\pi} \left| \frac{\epsilon - 1}{\epsilon + 2} \right| \tag{4.13}$$

[3]This theory is also commonly referred to as the Rayleigh-Gans-Debye (RGD) theory, or as the Born approximation (with analogy to quantum mechanics).
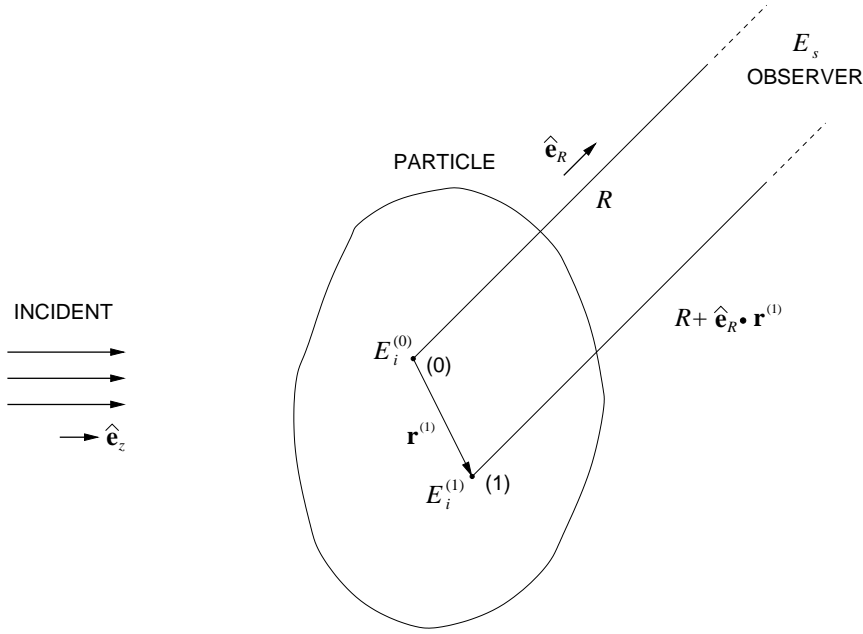
Figure 4.2: Illustration of contributions to the total scattered field at the observation point (distance R from the origin) from two volume elements: one labelled (0) at the origin, and the other labelled (1) at $\mathbf{r}^{(1)}$.

$$s_2 = -\frac{3ik^2}{4\pi}\left|\frac{\epsilon-1}{\epsilon+2}\right|\cos\theta \tag{4.14}$$

which we interpret as 'scattering matrix elements per unit volume'. The aim then is to integrate s_1 and s_2 (with an appropriate phase factor) over the volume of the particle, in order to approximate the total scattering matrix elements S_1 and S_2, and hence the radar cross section.

Consider a volume element labelled (0) at the origin (see figure 4.2) of volume dv, illuminated by an incident electric field $\begin{pmatrix} E_{i,\parallel}^{(0)} \\ E_{i,\perp}^{(0)} \end{pmatrix}$. The contribution to the parallel component of the scattered field from this element is:

$$dE_{s,\parallel}^{(0)} = \frac{\exp(ikR)}{-ikR}dv s_2 E_{i,\parallel}^{(0)}. \tag{4.15}$$

Now consider the volume element labelled (1), at position $\mathbf{r}^{(1)}$ relative to the origin. The contribution from this element is simply (4.15) modified by two phase factors: one for the change in position relative to the observer of $\exp(-ik\widehat{\mathbf{e}}_R \cdot \mathbf{r}^{(1)})$, and

another for the change in phase in the incident wave between the origin (0) and position (1) of $\exp(ik\widehat{\mathbf{e}}_z \cdot \mathbf{r}^{(1)})$. We neglect any coupling between (0) and (1). The contribution from element (1) is therefore:

$$dE_s^{(1)} = \frac{\exp(ikR)}{-ikR} dv s_2 E_{i,\parallel}^{(0)} \exp(ik\mathbf{r}^{(1)} \cdot (\widehat{\mathbf{e}}_z - \widehat{\mathbf{e}}_R)). \tag{4.16}$$

Similar arguments may be applied for the perpendicular component $d\mathbf{E}_{s,\perp}$. Integrating over the particle volume, the total scattered field is then:

$$\begin{pmatrix} E_{s,\parallel} \\ E_{s,\perp} \end{pmatrix} = \frac{e^{ik(R-z)}}{-ikR} \begin{pmatrix} S_2 & 0 \\ 0 & S_1 \end{pmatrix} \begin{pmatrix} E_{i,\parallel} \\ E_{i,\perp} \end{pmatrix}, \tag{4.17}$$

and the scattering matrix elements are:

$$S_1 = -\frac{3ik^2}{4\pi} \left| \frac{\epsilon - 1}{\epsilon + 2} \right| \int_v e^{i\delta} dv \tag{4.18}$$

$$S_2 = -\frac{3ik^2}{4\pi} \left| \frac{\epsilon - 1}{\epsilon + 2} \right| \cos\theta \int_v e^{i\delta} dv \tag{4.19}$$

where $\delta = k\mathbf{r} \cdot (\widehat{\mathbf{e}}_z - \widehat{\mathbf{e}}_R)$. In this approximation then, the scattering by an arbitrarily shaped particle may be calculated, and in the remainder of this chapter, we apply this methodolgy to estimate the radar cross section of snowflake aggregates. In this scenario $\theta = \pi$, and $\delta = 2k\mathbf{r} \cdot \widehat{\mathbf{e}}_z$. Using the matrix elements above, the radar cross-section of a snowflake of mass m is given by:

$$\sigma_r = \left[\frac{36\pi^3}{\rho_{ice}^2} \left| \frac{\epsilon - 1}{\epsilon + 2} \right|^2 \lambda^{-4} \right] m^2 f, \tag{4.20}$$

where

$$f = \left[\frac{1}{v} \int_v \exp(2ki\mathbf{r} \cdot \widehat{\mathbf{e}}_\mathbf{z}) dv \right]^2 \tag{4.21}$$

and ρ_{ice} and ϵ are the density and dielectric constant of (solid) ice respectively. The form factor f represents the deviation from the Rayleigh regime as the size of the particle and the wavelength of the incident light become comparable. In the Rayleigh limit $f = 1$; as r increases relative to λ, the form factor falls off with a functional dependance which, in general, depends on the geometry of the particle whose volume is being integrated over in equation 4.21.

As discussed above, the Rayleigh-Gans theory neglects coupling between the elemental scatterers, and this places limits on its applicability. In particular, Bohren

and Huffman (1983) quote the conditions $|\sqrt{\epsilon} - 1| < 1$, $|\sqrt{\epsilon} - 1|kr < 1$. For fractal aggregates however, Berry and Percival (1986) have shown that these conditions may be significantly relaxed. Their calculations show that because of the open structure, multiple scattering between the monomer particles composing fractals with $d_f \leq 2$ is negligible, irrespective of the overall size of the aggregate, and for $d_f > 2$ only becomes significant when the number of monomers composing the aggregate becomes of order $(kr_0)^{-d_f/(d_f-2)}$ (where r_0 is the size of the monomers). So provided that multiple scattering within the monomers themselves is negligible (ie. $|\sqrt{\epsilon} - 1|kr_0 < 1$), which we expect to be reasonable for typical radar frequencies/monomer sizes, the Rayleigh-Gans theory may be safely employed.

The monomer geometry may also play a role in determining the range of applicability of the Rayleigh-Gans theory. Since all interaction between the scatterers (which are assumed to act as equivalent volume Rayleigh spheres) is neglected, any polarisability of the monomer particles is implicitly neglected. However, Liu and Illingworth (1997) have studied the scattering from a quite elongated hexagonal ice crystal (aspect ratio=3), and found that for $kr_0 \ll 1$ an equivalent volume sphere gives the same results to within 1%. We therefore expect that ignoring the polarisability of the monomer particles is an acceptable approximation, provided that they are much smaller than the incident radar wavelength.

4.3.1 Radar cross section of a single snowflake

In this section we calculate the radar cross sections of our simulated snowflakes, and compare them to analytic results from the literature. It is apparent from equations 4.20 and 4.21 that the scattering cross section is sensitive to particle shape through the form factor f. In figure 4.3, we show the form factor calculated from our simulation clusters. Equation 4.21 was evaluated (numerically) for each cluster produced over the course of the simulation, at a range of different wavelengths. The resulting values of f were binned as a function of $(2kr)$ and averaged to yield the curve shown in figure 4.3. The plot shown is for a simulation run to an average cluster size of $s(t) = 50$; however f was also calculated for runs continuing to $s(t) = 400$
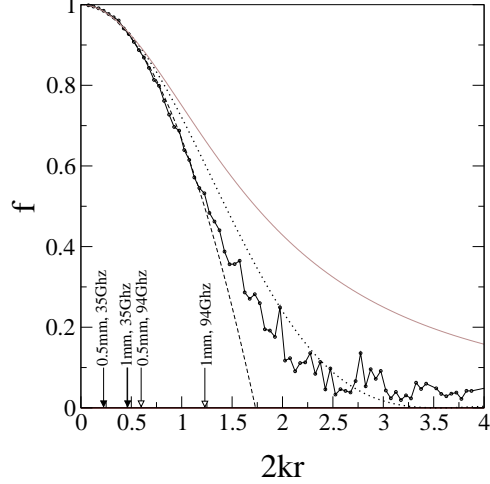
Figure 4.3: Form factor for simulated aggregates (points) as a function of size (relative to wavelength). Dashed line is the Guinier approximation. Dotted line shows the form factor for a sphere with the same radius of gyration. Grey line is the result of Berry and Percival (1986). Equivalent values of $2kr$ for snowflakes of diameter 0.5 and 1.0 mm at 35 and 94 Ghz are marked on the axis.

and the resulting plot was almost identical. The geometry of the monomer particles was also varied, using column shaped crystals with aspect ratios between 1 and 10, and again the form factor was unchanged to within the estimated error. This result seems sensible, since the shape of the curve depends only on the statistics of the cluster geometry, which were shown in chapter 2 to be universal.

Analytic approaches to calculating the form factor are based on a recognition that f is essentially the Fourier transform of the two point density correlation function introduced in chapter one. Assuming isotropy (or averaging over different orientations), the probability density $P(\Delta)$ of finding a pair of particles separated by a distance Δ is given by:

$$P(\Delta) = \frac{1}{4\pi} r^{-3} \Psi(\Delta/r) \tag{4.22}$$

where $\Psi(x) = x^{d_f - 3} h(x)$, $x = \Delta/r$ and the cut-off function $h(x)$ describes the edge of the fractal. The form factor is then given by (eg. Sorensen 2001):

$$f(2kr) = \int x^2 \Psi(x) \frac{\sin\left(2\sqrt{2}krx\right)}{2\sqrt{2}krx} \mathrm{d}x. \tag{4.23}$$

55

From the above, it is apparent that if the cut-off function $h(x)$ (and hence $\Psi(x)$) is known, then the form factor f may (in principle) be calculated exactly. This is the approach taken by Berry and Percival (1986), who assumed a simple exponential for h, and obtained:

$$f = \frac{\sin\{(d_f - 1)\tan^{-1}[2\sqrt{2}kr/b]\}}{(d_f - 1)(1 + 8k^2r^2/b^2)^{(d_f-1)/2}2\sqrt{2}kr/b} \tag{4.24}$$

where $b = \sqrt{d_f(d_f + 1)}$. For a fractal dimension of 2 (as predicted by our theory for snowflakes in an inertial regime), equation 4.24 simplifies dramatically, to give:

$$f = \frac{1}{1 + \frac{1}{3}(2kr)^2}. \tag{4.25}$$

This function is plotted alongside our simulation data in figure 4.3. At small sizes ($2kr < 0.5$) the agreement is good; however as the aggregate size becomes more comparable with the wavelength, the Berry and Percival formula significantly overestimates the form factor (and hence the back scatter). An exponential form for $h(x)$ then would appear to be a poor approximation for our aggregates, and indeed this has been found by researchers studying other fractal aggregates, in laboratory studies of soot (Sorensen *et al* 1992) and in numerical studies of diffusion- and reaction-limited cluster-cluster aggregates (Lin *et al* 1990). In both cases it was found that a sharper cut-off than the simple exponential was needed to acceptably describe the data.

Other analytical expressions for f have also been derived. In meteorological studies of radar scattering, snowflakes are often approximated by spheres, in order to utilise the exact solution of Mie (1908). The form factor (4.21) for a sphere may be calculated analytically:

$$f = \left[\frac{3}{u^3}(\sin u - u\cos u)\right]^2 \tag{4.26}$$

where $u = 2\sqrt{5/3}kr$. Matrosov (1992) demonstrated that for typical combinations of snowflake size and radar wavelength the Rayleigh-Gans approximation closely mimics the full Mie solution.

From figure 4.3 it is apparent that, as in the case of the Berry & Percival formula, the correspondence between the sphere and our aggregates is quite good

at small enough sizes, but diverges once $2kr > 0.5$. We also note that the sphere model predicts a form factor of zero (ie. no back scatter at all) at $2kr \simeq 3.5$, and similar points with $f = 0$ at higher values of $2kr$. This undulating form (also found in the exact Mie solution) is a peculiarity of the spherical case, and is not reproduced for our aggregates which do not possess the smooth, symmetrical shape of the idealised dielectric sphere. The errors associated with the spherical approximation are discussed in more detail in section 4.7.

It was noted above that the exact shape of the form factor f is sensitive to the form of the correlation function $\Psi(x)$. However, Guinier (Guinier 1939, Guinier *et al* 1955) showed that the *asymptotic* behaviour at small $2kr$ is independent of particle shape. Expanding $x^{-1}\sin(x) \simeq 1 - \frac{1}{6}x^2$ and changing variables, he found:

$$f \simeq 1 - \frac{1}{3}(2kr)^2 \qquad \text{as } (2kr) \to 0. \qquad (4.27)$$

This asymptotic form is known as the Guinier regime and applies to particles of any shape, provided that $2kr$ is small enough for the higher order terms in the expansion to be neglected. Equation 4.27 is plotted in figure 4.3, and proves to be an excellent fit to our simulation data up to $2kr \simeq 1$, beyond which the Guinier result underestimates the aggregate curve. We note that Guinier underestimates the sphere and Berry/Percival fractal much earlier ($2kr \simeq 0.5$). We attribute this extended agreement to a much sharper cut-off $h(x)$ in the probability density for our aggregates, resulting in a more rapid fall off in the form factor.

Values of $2kr$ for typical Cirrus snowflake sizes (0.5 and 1mm diameter) at representative radar frequencies (35 and 94 Ghz) are marked on figure 4.3, and in all cases $2kr < 1$ (the Guinier regime). We investigate the consequences of this in the next section, where we show if the Guinier approximation holds, derivation of average particle size is exceptionally straightforward, and may be achieved through a simple analytical formula.

Since radar scattering is rather sensitive to the largest particles in the distribution (even though there may be relatively few of them), we also consider the case of snowflakes beyond the Guinier regime and fit a curve to the complete form

57

factor shown in figure 4.3. We then demonstrate how such a curve may be used to interpret radar data which is outside the Guinier regime.

4.4   Interpretation of reflectivity data

In this section we employ the dynamical scaling property of the distribution, along with the results from the previous section on the scattering from individual snowflakes, in order to study the physical significance of reflectivity measurements and to make use of this understanding to infer the cloud's microphysical properties (average snowflake size, ice water content, etc).

Having calculated the form factor f, equation 4.20 may be evaluated for each snowflake in the scattering volume and the results added up, to obtain the reflectivity (defined in section 4.2):

$$\eta = c \left[\frac{\sum m^2 f(2kr)}{\lambda^4} \right] \tag{4.28}$$

where the constant $c = 36\pi^3 |\frac{\epsilon-1}{\epsilon+2}|^2 / \rho_{ice}^2$. Multiple scattering between the snowflakes themselves is assumed to be negligible, given the dilute nature of most ice clouds. Note that in the meteorological literature, the reflectivity is commonly rescaled to give the 'radar reflectivity', defined as $Z = \lambda^4 \pi^{-5} \left| \frac{\epsilon-1}{\epsilon+2} \right|^{-2} \eta$. In this thesis we will use η for clarity, since its definition follows naturally from the radar cross sections calculated in the previous section.

4.4.1   The Rayleigh limit

We consider first the case of the Rayleigh regime where the wavelength is much longer than the size of the particle. As a result the form factor $f = 1$, and the reflectivity is simply:

$$\eta = \frac{c \sum m^2}{\lambda^4}. \tag{4.29}$$

Thus in the Rayleigh limit, the reflectivity provides a measure of the second moment of the mass distribution $M_2 = \sum m^2$. Numerous studies in the meteorological literature have attempted to link reflectivity from a single radar scattering in the

58

Rayleigh regime directly to the ice water content (IWC) through empirical studies. However, equation 4.29 immediately highlights the futility of such an approach: in the Rayleigh regime the reflectivity is sensitive to the second moment M_2, whereas IWC is the total mass (per unit volume) $= M_1 = \sum m$. Recall that in chapter two we defined the average cluster mass $s(t) = M_2/M_1$; from this, it is apparent that in the Rayleigh limit:

$$\text{IWC} = \frac{\sum m^2}{s} = \frac{\eta \lambda^4}{cs}. \tag{4.30}$$

In order to estimate IWC then, some estimate (or prescription) for the average snowflake mass s is needed. Clearly s depends on the weight of the pristine ice crystals that make up the aggregate and on how far the aggregation itself has proceeded, both of which vary considerably from cloud to cloud. As a result it is expected that the parameters in the empirical fits relating reflectivity to IWC will also vary considerably, and this is born out in the results from the literature. To accurately infer ice water content from radar reflectivity in the Rayleigh regime then, a means of estimating the average snowflake size $s(t)$ is also required.

4.4.2   The Guinier regime

We now consider the case where the scattering from the snowflakes falls within the Guinier regime $(2kr < 1)$, and $f \simeq 1 - \frac{1}{3}(2kr)^2$. In this case the reflectivity is given simply by:

$$\eta = c \left[\frac{\sum m^2}{\lambda^4} - \frac{16\pi^2}{3} \frac{\sum m^2 r^2}{\lambda^6} \right]. \tag{4.31}$$

The first term in the bracket is the Rayleigh result (as in section 4.4.1), and for long enough wavelengths (compared to r) this behaviour dominates the scattering. As wavelength and particle size become more comparable the second term becomes more significant, and the scattering becomes directly dependent on the particle radius (as opposed to the Rayleigh limit, where the only dependence is on particle mass). The implication is that if more than one radar wavelength is used, an estimate of average particle radius may be obtained. Given equation 4.31, a natural definition for the average particle radius is $r_{av} = [\sum m^2 r^2 / \sum m^2]^{\frac{1}{2}}$, and for two reflectivity

measurements η_1 and η_2 (at wavelengths λ_1 and λ_2) we find:

$$r_{av} = \left[\frac{3}{16\pi^2} \cdot \frac{1 - \beta}{1/\lambda_1^2 - \beta/\lambda_2^2} \right]^{1/2} \tag{4.32}$$

where $\beta = (\eta_1 \lambda_1^4)/(\eta_2 \lambda_2^4)$, or in terms of radar reflectivities $\beta = Z_1/Z_2$.

The practical upshot of equation 4.32 is that given two simultaneous measurements at different radar frequencies the average snowflake radius may be calculated *analytically*, provided that a) at least one of the radars is operating at a wavelength sufficiently short that some of the snowflakes fall outside the Rayleigh regime, and b) both radars have wavelengths long enough that the snowflakes fall predominantly inside the Guinier regime ($2kr < 1$). In previous dual wavelength studies (eg. Matrosov 1998, Hogan and Illingworth 2000), the relationship between average particle size and β has been calculated numerically for spheres and ellipsoids; here we have a simple analytic result, which we expect to be applicable to typical snowflake sizes and radar wavelengths.

Once r_{av} has been calculated then either of the reflectivity measurements may be used to infer M_2. Rearranging equation 4.31 yields:

$$\sum m^2 = \frac{\eta \lambda^4}{c \left[1 - \frac{1}{3}(2kr_{av})^2 \right]}. \tag{4.33}$$

This would appear to resolve the problems discussed in the Rayleigh case, since we now have an estimate of average particle size and M_2. However, it is an average *radius* that has been derived as opposed to the average mass $s(t)$, and some conversion between the two is required. From our results in chapter two however, we know that

$$m = ar^{d_f} \tag{4.34}$$

where our theory and experimental relationships lead us to expect a fractal dimension $d_f = 2$ which is universal, and this in agreement with experimental data. However, the prefactor a depends on the mass (m_0) radius (r_0) and shape (through the dimensionless parameter γ) of the pristine particles that make up the aggregate: $a = \gamma m_0 / r_0^{d_f}$. With no prior knowledge of the shape and size of the pristine ice crystals at the top of the cloud, it is not possible to convert r_{av} to s.

If some estimate or prescription for a is available, then we may use the dynamical scaling property of the mass distribution to infer $s(t)$. Using the fractal scaling (with $d_f = 2$) and the moment equation (2.11) we find:

$$s(t) \;=\; a \left(\frac{p_2}{p_{2+2/d_f}} \right)^{d_f/2} r_{av}^{d_f} \tag{4.35}$$

$$\;=\; a \frac{p_2}{p_3} r_{av}^2 \qquad \text{for } d_f = 2 \tag{4.36}$$

where the p_n are the moments of the rescaled distribution $\phi(m/s)$. The ratio p_2/p_3 is anticipated to be universal, and in our simulations we find that the ratio asymptotes to a value of around 0.43 ± 0.01. An estimate of p_2/p_3 from the *experimental* size distributions may also be obtained. Using the data from section 2.4 and assuming $d_f = 2$, a value of 0.44 ± 0.02 may be inferred, in close agreement with our simulations — for full details see appendix B. Once $s(t)$ has been derived from r_{av} then, the ice water content may be derived without ambiguity through IWC $= M_2/s$.

4.4.3   Larger aggregates

For $2kr > 1$ the Guinier formula breaks down, and in this section we use our simulation data to fit a curve that describes the scattering at large sizes. Equation 4.28 may be re-written in the form:

$$\eta = c \left[\frac{M_2 \mathcal{F}(2kr_{av})}{\lambda^4} \right] \tag{4.37}$$

where $\mathcal{F} = \sum m^2 f / \sum m^2$ (ie the m^2 weighted average of the form factor f) which, given the fractal geometry and dynamical scaling of the distribution, we expect to be a (universal) function of $2kr_{av}$. We therefore calculate $\mathcal{F}$ in our simulations, and attempt to fit a curve to the data. From the previous analysis we already know that in the small size limit $\mathcal{F} \simeq 1 - \frac{1}{3}(2kr_{av})^2$. At larger size parameters, more of the internal structure is visible to the radar, and it is well known (eg. Vicsek 1989) that for $2kr \gg 1$ (but where the wavelength is still larger than the size of the monomers), $f \sim (2kr)^{-d_f}$. Hence, for our aggregates we expect $\mathcal{F} \sim (2kr_{av})^{-2}$ in this regime, and we attempt to fit a function of the form:

$$\mathcal{F} = \frac{1 + c_1(2kr_{av})^2}{1 + (c_1 + \frac{1}{3})(2kr_{av})^2 + c_2(2kr_{av})^4} \tag{4.38}$$

61
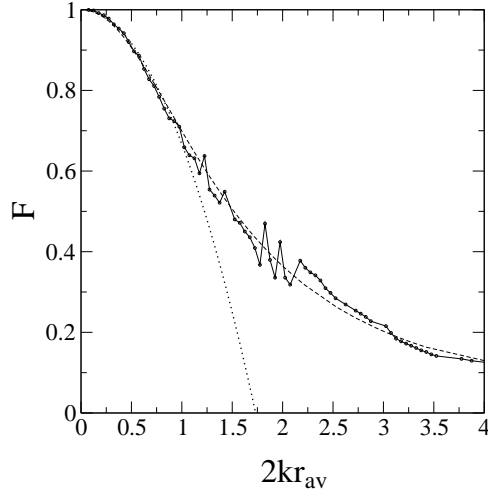
Figure 4.4: Plot showing the m^2-weighted average form factor $\mathcal{F}$, plotted as a function of $2kr_{av}$. Points are simulation data, dotted line corresponds to the Guinier approximation, dashed line shows the full fitted curve of equation 4.38.

which has the correct asymptotics in both limits. As shown in figure 4.4, this provides a good fit to the simulation data with $c_1 \simeq 12.7$ and $c_2 \simeq 3.6$. If the dual wavelength ratio $\beta = \mathcal{F}(2k_1 r_{av})/\mathcal{F}(2k_2 r_{av})$ is known, equation 4.38 may be used to obtain a cubic equation for r_{av}^2, and hence the average radius corresponding that value of β may be obtained: details are given in appendix C. Once r_{av} has been calculated then M_2 is simply $= \eta \lambda^4 / c\mathcal{F}(2kr_{av})$. The ice water content may be inferred using the same methodology described in section 4.4.2, through equation 4.36 and the relation IWC $= M_2/s$.

4.5   Inferring other microphysical quantities

Moments of the size distribution other than the ice water content may also be inferred from reflectivity measurements. In section 4.4 it was demonstrated that dual wavelength measurements of ice clouds allow the second moment M_2 to be measured, along with an average radius r_{av} which may be converted to an average mass s given knowledge of the prefactor a in the fractal scaling relation $m = ar^{d_f}$. We therefore wish to relate the moments of the size distribution that are of interest to the second moment (which we know). From the dynamical scaling of the distribution, it follows

62

that (see equation 2.11):

$$M_n = s^{n-2}\frac{p_n}{p_2}M_2. \tag{4.39}$$

provided $n > 0.6$ (this condition is due to the divergence of low moments, on account of the algebraic decay at small sizes $\phi(x \ll 1) \sim x^{-1.6}$ - see section 2.3.2 for details).

A moment of practical interest to the meteorologist is the precipitation rate $\mathcal{R} = \sum mv$. From chapter two, the snowflake fall speed is given by $v = \mathcal{K}m^\alpha/r$, where $\mathcal{K} = \kappa\nu_k^{1-2\alpha}(g/\rho)^\alpha$ and κ is a geometrical factor, which essentially relates the projected area to the square of the particle radius. In terms of M_2 and $s(t)$ then, we find that:

$$\mathcal{R} = \kappa a^{1/d_f} s^{\alpha - 1/d_f - 1}\frac{p_{1+\alpha-1/d_f}}{p_2}M_2. \tag{4.40}$$

This may also be expressed in terms of M_2 and the average *radius*, as derived from dual wavelength data (see section 4.4):

$$\mathcal{R} = \kappa a^{\alpha-1}\frac{p_{1+\alpha-1/d_f}}{p_2}\left(\frac{p_2}{p_{2+2/d_f}}r_{av}^2\right)^{\frac{1}{2}\{(\alpha-1)d_f-1\}}M_2 \tag{4.41}$$

We note that $\mathcal{R}$ is rather less sensitive to the value of the fractal scaling prefactor a than for the case of ice water content, scaling as $\sim a^{\alpha-1}$, as opposed to IWC $\sim a^{-1}$. We therefore expect that if a is simply prescribed rather than measured, then estimates of precipitation rate may more reliable than those of ice water content. The prefactor κ in the fall speed relation is also a function of the monomer geometry; how sensitive it is to the variation in crystal geometry observed in typical clouds is unclear, and merits further study.

Another parameter of interest to meteorologists which some authors have sought to derive from radar measurements is the effective radius r_e. This characterises the average ratio of volume to projected area (Foot 1988):

$$r_e = \frac{3}{2}\frac{\text{IWC}/\rho_{ice}}{\sum A} \tag{4.42}$$

where A is the particle projected area. We note however, that for aggregates, attempting to infer r_e from the dual wavelength derived average size is futile. Since the mass is proportional to r^2, and likewise for the projected area (the aggregates considered here are fractals with $d_f = 2$), the effective radius does not scale with

63

the radius of gyration or maximum dimension. Its value depends only on the details of the pristine particles that compose the aggregate. Although there is likely to be some correlation between r_{av} and r_e from cloud to cloud, this simply reflects the fact that larger pristine particles tend to yield larger aggregates. Trying to derive one radius from the other is not possible, and dual wavelength radar measurements therefore cannot be used to estimate r_e, since the back-scatter is sensitive to the overall aggregate size (r_{av}), rather than the details of the pristine particles.

4.6   Measuring average snowflake size in a cirrus cloud

In this section we apply the two methods of deriving average snowflake radius of section 4.4 to the dual wavelength radar data presented by Hogan and Illingworth (2000). Two radars operating at 35 and 94 Ghz (corresponding to wavelengths of 8.6 and 3.2 mm respectively) made vertically pointing reflectivity measurements of a thick cirrus cloud over Chilbolton in the UK. Figure 4.5.a) and b) show the radar reflectivities Z measured at both frequencies. The dual wavelength ratio β was then calculated, and is plotted in 4.5.c). This was then used to infer the average snowflake radius r_{av} using both the Guinier approximation as per equation 4.32, and the curve fitted to our simulation data as described in section 4.4.3. From figure 4.5.d) and e) it is apparent that there is little to separate the two results. The average radius r_{av} rarely exceeds 0.3mm, and so $2kr_{av} \leq 1.2$ at 94 Ghz and ≤ 0.4 for the 35 Ghz radar, hence the majority of the scattering is within the Guinier regime. For this kind of cirrus cloud then, the Guinier approximation provides a simple and accurate method of inferring average particle size; for thicker clouds where the aggregation has been allowed to continue for longer, the Guinier method may give incorrect results and the fitted curve of section 4.4.3 should provide a better approximation. However, both methods can only be properly validated by comparing radar derived values to direct measurements of the mass and radius distribution. Studies combining radar measurements with in-situ aircraft data from the cloud are needed in order to properly evaluate the accuracy of the inferred values of r_{av}.
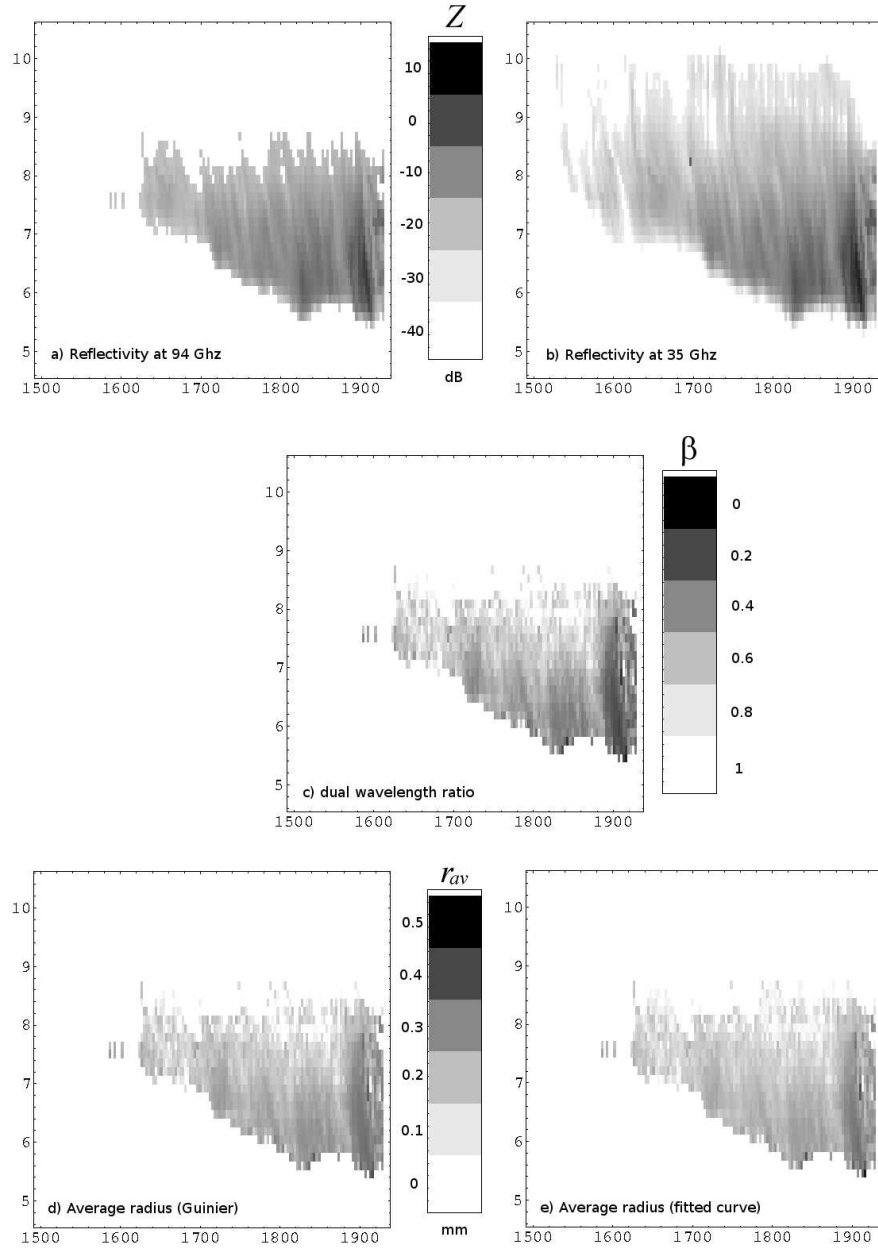
Figure 4.5: Time-series of dual wavelength radar data from a cirrus cloud over Chilbolton in the UK. In each plot the horizontal axis represents time, and the vertical axis height in kilometres. The radar reflectivity at 94 and 35 GHz are shown in panels (a) and (b) respectively. The scale is logarithmic, and is given by $Z[\mathrm{db}] = 10\log_{10} Z[\mathrm{mm}^6\mathrm{m}^{-3}]$. The ratio of the radar reflectivities β is shown in panel (c); we then plot the derived average radius r_{av} (in millimetres) using d) the approximate Guinier formula $\mathcal{F} \simeq 1 - \frac{1}{3}(2kr_{av})^2$, and e) the fitted curve from our simulation data (see text).
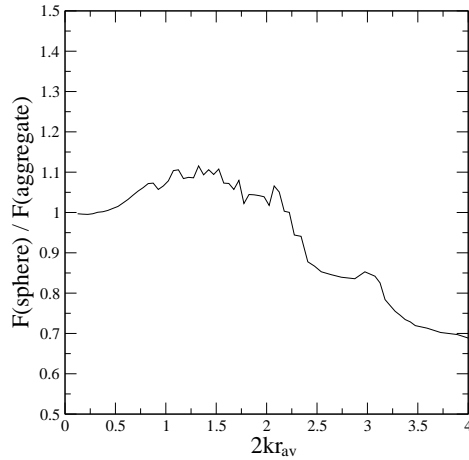
Figure 4.6: Plot showing ratio of the m^2 weighted average form factor of an equivalent sphere as compared to our simulated aggregates.

4.7   Comparison with spherical models

Many authors have used a spherical approximation when estimating the back scatter from snowflakes, modelling them as homogeneous mixtures of air and ice. The motivation for this kind of approximation is that the scattering from a sphere with a given diameter and dielectric constant may be calculated exactly using Mie theory. Here we consider how closely the spherical model matches the results from the Rayleigh-Gans theory.

To mimic the Rayliegh-Gans results for the radar cross section by our simulated aggregates using a sphere, we attempt to match up both the form factor f for the aggregates, and the m^2 dependence for $2kr \ll 1$. In figure 4.3 the form factor for a sphere was plotted alongside that for our simulated aggregates. There is good agreement up to $2kr \simeq 0.5$, after which the curves diverge somewhat. Thus for small aggregates at least, an equivalent sphere is an accurate representation provided that the mass and radius of gyration are conserved; the errors involved at larger sizes will be considered shortly.

We focus then on the regime $2kr < 0.5$. In order to match up the scattering from our sphere with that of the aggregate it is intended to model, we must ensure the radius of gyration of the sphere is the same as that of the aggregate. For

66

our simulated aggregates, the radius of gyration and maximum span are found to scale linearly with $r \simeq 0.3D$, whereas a sphere of diameter D_{sp} has $r = 0.39D_{sp}$ (eg. Goldstein 1980). To match these up then requires that the diameter of the equivalent sphere be $D_{sp} = 0.77D$. This ensures that the sphere has the same radius of gyration as the aggregate it is intended to represent, and hence the form factor shown in figure 4.3. A different choice of D_{sp} would result in the curve being squashed or stretched along the $2kr$ axis, and under/over-estimating the back scatter for $2kr < 0.5$.

To estimate the error involved in this approach, the scattering from our simulated distributions using the spherical form factor has been calculated. The ratio of the m^2 weighted form factor $\mathcal{F}$ for the sphere model and true aggregates, is plotted in figure 4.6. Up to $2kr_{av} \simeq 2$ the error in $\mathcal{F}$ is less than 10% (equivalent to an average maximum span of 1.5mm at 94Ghz, or 4.0mm at 35GHz); at larger sizes, the error increases, and at $2kr_{av} = 4$, the sphere model underestimates the aggregate by around 30%.

The second dependence that must be matched is the snowflake mass. Since the snowflakes are not solid ice spheres, information about how much of the mixture is air and how much is ice must be introduced by using an 'average' dielectric constant ϵ_{av} weighted by the volume fraction of ice in the sphere $f_v = m/\frac{\pi}{6}(D_{sp})^3\rho_{ice}$. The most common prescription for ϵ_{av} is the Maxwell-Garnett (1904) formula:

$$\epsilon_{av} = \frac{1 - f_v + \epsilon \zeta f_v}{1 - f_v + \zeta f_v} \tag{4.43}$$

where the parameter ζ reflects the distribution of sizes and shapes of the ice 'inclusions' in the mixture (see Bohren and Huffman 1983 for more details). For spherical inclusions $\zeta = 0.58$. To check that introducing the aggregate density in this way yields the same m^2 dependence as per equation 4.20, we study the Rayleigh limit where the back scatter cross section of our equivalent sphere is given by (see equations 4.11 and 4.12):

$$\sigma_r = \frac{\pi^5}{\lambda^4}\left|\frac{\epsilon_{av} - 1}{\epsilon_{av} + 2}\right|^2 D_{sp}^6. \tag{4.44}$$

For solid ice spheres $\epsilon_{av} = \epsilon$, and since $m = \frac{\pi}{6}(D_{sp})^3\rho_{ice}$, one recovers equation
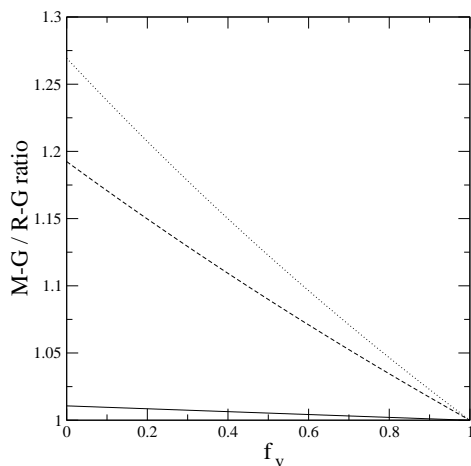
Figure 4.7: Ratio comparing the back scatter cross section calculated using the Maxwell-Garnett sphere model, and the Rayleigh-Gans theory, for $2kr \ll 1$ (the Rayleigh limit). Solid line represents spherical inclusions ($\kappa = 0.58$), dashed is Meneghini and Liao ($\kappa = 0.63$), and dotted is rod shaped inclusions ($\kappa = 0.65$).

4.20 with $f = 1$. For small volume fractions (the case most relevant to fractal aggregates, since the overall density is proportional to $r^{d_f - 3}$) we calculate the ratio of the back scatter obtained from equation 4.44 to that obtained from equation 4.20 as a function of the volume fraction f_v: in the Rayleigh limit this turns out to be simply $|\frac{\epsilon_{av} - 1}{\epsilon_{av} + 2}|^2 / \{|\frac{\epsilon - 1}{\epsilon + 2}|^2 f_v^2\}$. This ratio is unity at $f_v = 1$; even as $f_v \to 0$ the error is only around 1% (see figure 4.7). Other values of the parameter ζ are also in common usage - the assumption of needle shape inclusions gives $\zeta = 0.65$ and Meneghini and Liao (1996) have proposed a value of $\zeta = 0.63$. These alternate values of ζ essentially represent the polarisability of the inclusions (which we interpret in the case of our aggregates as being the monomer particles), and they predict a back scatter increased by as much as 25% as $f_v \to 0$, as shown in figure 4.7. In section 4.3 it was commented that in the Rayleigh limit the scattering from the individual monomers should be well represented by a sphere of the same volume. If this is the case then the Rayleigh-Gans approximation ought to be accurate, and these two values of ζ overestimate the scattering quite significantly, particularly at low volume fractions.

In summary, the spherical approximation matches the results for our aggre-

gate snowflakes provided that i) the diameter is chosen so as to match the radius of gyration of the sphere to the snowflake it is intended to model, and ii) the parameter ζ is chosen so as to give the correct m^2 dependence in the Rayleigh limit. If the size of the aggregates is not too close to the wavelength of the radar, then the errors involved in modelling aggregates as air/ice spheres are only 10% or so; for larger aggregates this may increase to 30% or more.

4.8   Conclusions

The radar cross sections for our simulated snowflakes have been calculated using the Rayleigh-Gans theory by treating the aggregates as being an assembly of independent Rayleigh scatterers, and summing up the contributions from each element in that assembly. In this theory, the scattering is proportional to the square of the particle mass (as in the Rayleigh limit) and the form factor f, a dimensionless function which describes the depedence on particle size and geometry. This function is universal (ie. independent of the size and shape of the monomer particles), and f has been calculated for our simulated aggregates.

The form factor for our simulated snowflakes was compared to analytical results for f from the scattering literature, the most successful of which in describing the data was the Guinier result $f = 1 - \frac{1}{3}(2kr)^2$, which fits our data well up to $2kr \simeq$ 1. Berry and Percival's (1986) result overestimates the back scatter considerably for $2kr > 0.5$, and this is believed to be the result of their assumption of an exponential cut-off in the density correlation function. The form factor for a sphere is also found to overestimate the back scatter, albeit to a lesser extent.

Having calculated the scattering cross section of individual aggregates, these were then integrated over the size distribution, and the results interpreted in terms of moments of that distribution. The reflectivity is proportional to the second moment of the mass distribution M_2 and the average form factor $\mathcal{F} = \sum m^2 f / \sum m^2$. We have calculated $\mathcal{F}$ as a function of the average radius r_{av}, and fitted a curve to our simulation data.

The application of our results to the inference of average snowflake size from radar data has been investigated, and for snowflakes sufficiently small compared to the wavelength, the Guinier approximation provides a very simple analytic expression for r_{av} in terms of the dual wavelength ratio β. At larger values of $2kr_{av}$, the Guinier curve underestimates the back scatter, and the full fitted curve of section 4.4.3 must be used to interpret the data, as described in appendix C.

Ideally, we would like to interpret the radar reflectances in terms of the ice water content (total mass per unit volume) in the cloud. Since reflectivity is proportional to $\sum m^2$, some measure of average mass is required. We have shown that it is possible to derive the average particle radius r_{av} from dual wavelength radar data and this may be converted to an average mass, provided that the prefactor in the fractal scaling $m = ar^{d_f}$ is known: a is a function of the monomer particle size and geometry.

Radar data may also be interpreted in terms of further moments, such as the precipitation rate $\sum mv$. We have shown that the dependence of $\mathcal{R}$ on a is not as strong as for IWC. However, the inclusion of particle fall speed v in this moment means that an additional dependence on the shape of the monomer particles is introduced, and the overall sensitivity of $\mathcal{R}$ to the geometry of the ice crystals composing the aggregate is unclear at present.

Some authors have attempted to derive the effective radius (characterising the ratio of particle volume to projected area) from radar measurements. However we have shown that r_e depends only on the monomer particles (to which the radar is insensitive) and not the overall size of the aggregate as characterised by r_{av}. Direct inferral of r_e then is not possible from dual wavelength radar data.

Finally, the errors involved in modelling our simulated snowflakes as air/ice spheres using the Maxwell-Garnett mixture theory was analysed. It was found that provided some care was taken in constructing the equivalent sphere, and the radius is not too large ($2kr_{av} < 2$), the error is less than 10%. This error increases to around 30% at larger sizes ($2kr_{av} \simeq 4$).

Chapter 5

Discussion and conclusions

Our computer simulations have demonstrated that clusters produced by differential sedimentation of particles in a fluid are statistically self-similar in their geometry, with a fractal dimension governed by the drag regime, and independent of the monomer crystal type or size. Our theoretical arguments lead us to believe that the system self-organises so as to sit on the margin between regular growth and a run-away regime: this has allowed us to make a theoretical prediction of the fractal dimension $d_f = \max\{2, 1/(1-\alpha)\}$, for $\alpha < \frac{2}{3}$. For a purely inertial flow ($\alpha = \frac{1}{2}$) the fractal dimension is $d_f = 2$ in strong agreement with experimental data on aggregate snowflakes. For viscous fluid flows ($\alpha > \frac{2}{3}$), the theoretical prediction is $d_f = 3$ and run-away growth, although our model does not account for viscous effects like the sweeping of small clusters around larger ones; this regime merits further study. The aspect ratio of our simulation clusters has also been measured, and is found to approach a universal asymptote of $\simeq 0.65 \pm 0.05$ for $\alpha = \frac{1}{2}$, in good agreement with aircraft image data.

The distribution of clusters by size was found to scale dynamically, being described by a single function ϕ which is rescaled as the aggregation proceeds: $n(m,t) = s(t)^{-\xi}\phi(m/s)$. Size distributions from both our simulated clusters, and from aircraft measurements were found to conform to this scaling behaviour. The shape of the underlying distribution $\phi(x)$ has been studied at small and large sizes: at small $x = m/s$, a power law $x^{-\tau}$ is dominant with $\tau \simeq 1.6 \pm 0.1$; at larger

cluster sizes there is an exponential cut-off. Theoretical expectations back this up, predicting a similar power law with $\tau < 2$ for small x, and a function of the form $\sim x^{-\theta} \exp(-\delta x)$ at large x. The exponents τ and δ are sensitive to the detailed form of the collision kernel, and cannot (to the author's knowledge) be calculated without the complete solution of the Smoluchowski equations. The exponent θ may however be calculated by solution of a transcendental equation $J(\theta) = 0$ (see chapter 3). This equation (in general) has more than one root, and it is unclear which one the system will pick; in the inertial limit however, it appears that these converge to a single root at $\theta = 1.5$.

In the final chapter of this thesis, the implications of fractal geometry and a dynamically scaling size distribution on the radar scattering properties of our synthetic snowflakes were considered. Using the Rayleigh-Gans theory, we show that the effect of the cluster geometry on the scattering is described by a universal dimensionless function (the form factor f). This function has been calculated for our simulation clusters, and provided that the monomer particles are small compared to the incident wavelength, f is independent of their shape or size. Our calculated form factor is well approximated by the analytical result of Guinier up to $2kr \simeq 1$, and by Berry & Percival's formula up to $2kr \simeq 0.5$. The homogeneous sphere approximation was considered in detail on account of its ubiquity in the meteorology literature, and the errors involved were estimated to be around 10% as long as the correct radius $(= 0.77D)$ is chosen, and the snowflakes are not too large.

Our results on the scattering properties of single snowflakes were then applied to the problem of interpreting radar returns from the complete distribution of snowflakes inside the scattering volume. We find that dual-wavelength radar data allows the estimation of average snowflake radius r_{av} and of the second moment of the mass distribution M_2; in the Guinier regime this procedure is particularly simple. In order to infer properties of interest such as ice water content, an average cluster mass s is needed, and although we know $s \sim r_{av}^2$, the prefactor remains dependent on the monomer crystal size and geometry, which are unknown. In short, without some prescription or alternative measurement of the monomer ice particles,

dual wavelength data alone does not give sufficient information to unambiguously infer ice water content or precipitation rate.

We appear to have a fairly complete understanding of the geometry of aggregates formed by differential sedimentation of particles, in particular snowflakes formed by collision of snow crystals in ice clouds. The correspondence between our results and experimental data indicates that the details of the sticking mechanism are not strongly size-dependent, and may be neglected at this level of theoretical model; however further theoretical and laboratory work are needed to verify the validity of this assumption. In addition the assumption of random cluster reorientation between collisions is clearly overly simplistic: experimental data on the distribution of canting angles as a function of snowflake size is needed to test the sensitivity of our results to this assumption. Preliminary simulation results with biased cluster orientation appear to indicate that the fractal dimension and dynamical scaling properties are preserved, with a slight variation in the aspect ratios for the strictest reorientation scheme. This is an area that requires further investigation.

Our success in rescaling experimental size distributions onto a universal curve indicates that there is a single dominant aggregation mechanism at play - however the 'kink' at small snowflake sizes indicates that we may not have captured its form exactly. Possible candidates for the source of this feature include fluid effects not included in our model, such as small clusters being swept around larger ones or wake capture. Another possibility is that the growth of smaller clusters is not entirely dominated by aggregation, and some diffusional growth may also be occurring. This issue remains unresolved and is an avenue for future research.

Other issues which have not been addressed in this thesis are the breakup of snowflakes and their riming. The former may perhaps be a candidate for the 'kink' in the distribution, favouring as it does an increased population of smaller flakes. In the latter case, where falling snowflakes collide with supercooled water drops, we intuitively expect the riming to mirror ballistic particle-cluster aggregation, since the drops are generally much smaller than the flakes. This would lead to rather more compact structures, with a higher fractal dimension than our 'dry snowflake'

73

model predicts.

In summary, a theoretical model of snowflake aggregation in ice clouds has been constructed, simulated on computer, and analysed in terms of the Smoluchowski equations. Good agreement was found with experimental data, and we believe that the model has captured the universal features of snowflake formation, although some questions still remain unanswered. The radar scattering from snowflakes has been investigated using the Rayleigh-Gans theory, and the results clarify the interpretation of dual-wavelength radar returns from ice clouds. We also hope that in the future our results may help to produce more accurate estimates of the optical and infra-red light scattering from ice clouds, so that their effect on the earth's radiation budget and global warming may be understood. Most importantly however, we have shown that despite their well recorded variety in size and shape, snowflakes have universal features governed by the physics of the aggregation and not the details of the pristine snow crystals that make them up. Understanding what is universal (and what is not) is crucial if we are to understand the role snowflakes play in our atmosphere, and it is hoped that this thesis will go some way towards improving that understanding.

Appendix A

Scaling of the experimental cluster span distribution

Here we present details of how the bin-width particle span distributions may be rescaled. The mass distribution may be written as:

$$\frac{\mathrm{d}N}{\mathrm{d}m} = s^{-\xi}\phi(m/s) \tag{A.1}$$

as detailed in section 2.3. We now assume the fractal scaling $m = aD^{d_f}$ holds, where a is a constant. Then the distribution by cluster span D is given by:

$$\frac{\mathrm{d}N}{\mathrm{d}D} = ad_f D^{d_f-1}s^{-\xi}\phi(m/s). \tag{A.2}$$

From this, the moments of the D-distribution $\mathcal{M}_k$ may be calculated:

$$\mathcal{M}_k = \int_{D_s}^{\infty} \frac{\mathrm{d}N}{\mathrm{d}D}D^k\mathrm{d}D \tag{A.3}$$

$$= s^{-\xi+1+k/d_f}a^{-k/d_f}\int_{x=1/s}^{x=\infty} x^{k/d_f}\phi(x)\mathrm{d}x \tag{A.4}$$

where D_s is the span of the smallest monomer particle ($m = 1$). To avoid the divergence described in section 2.3 (on account of the anticipated power law decay at small sizes $\phi \sim x^{-\tau}$), we choose moments $k > d_f(\tau-1)$ to construct the characteristic cluster span D_{av}. Since we measure $\tau \simeq 1.6$ and $d_f \simeq 2$, the second moment $\mathcal{M}_2$ is the lowest integer moment which is not dominated by the small size cut-off, and scales

in the desired manner. We therefore take $D_{av} = \mathcal{M}_3/\mathcal{M}_2 = (s/a)^{1/d_f}(P_{3/d_f}/P_{2/d_f})$ (the P's are moments of ϕ - see section 2.3). Normalising A.2 by $\mathcal{M}_2$ then:

$$\mathcal{M}_2^{-1}\frac{\mathrm{d}N}{\mathrm{d}D} = D_{av}^{-3}\frac{d_f}{P_{2/d_f}}\left(\frac{D}{D_{av}}\right)^{d_f-1}\left(\frac{P_{2/d_f}}{P_{3/d_f}}\right)^{d_f+2}\phi\left[\left(\frac{P_{3/d_f}D}{P_{2/d_f}D_{av}}\right)^{d_f}\right] \tag{A.5}$$

It is therefore possible to rewrite equation A.2 in terms of the average span D_{av}, along with a universal function ψ which is dimensionless and depends on D/D_{av} alone:

$$\mathcal{M}_2^{-1}\frac{\mathrm{d}N}{\mathrm{d}D} = D_{av}^{-3}\psi(D/D_{av}) \tag{A.6}$$

which is the form used in section 2.4 to rescale our experimental and simulation data. Equation A.6 may also be generalised to employ higher moments of the distribution:

$$\mathcal{M}_k^{-1}\frac{\mathrm{d}N}{\mathrm{d}D} = G_k^{-1}L_k^{-(1+k)}\left(\frac{G_{k+1}}{G_k}\right)^{1+k}\psi\left(\frac{D}{L_k}\frac{G_{k+1}}{G_k}\right) \tag{A.7}$$

where the characteristic cluster span $L_k = \mathcal{M}_{k+1}/\mathcal{M}_k$, and the G_k are (dimensionless) moments of the universal distribution ψ.

Appendix B

Using the experimental size distributions to infer p_2/p_3

Here we show how the ratio p_2/p_3 (the second and third moments of the rescaled *mass* distribution ϕ) is calculated from the experimental particle *span* distributions. Using equation 1.2 one can write the moments of the radius distribution as:

$$\mathcal{M}_n = \int_0^\infty (m/a)^{n/d_f} n(m,t) dm \qquad (B.1)$$

which, using the dynamical scaling property (2.9), and taking $d_f = 2$ is:

$$\mathcal{M}_n = (s/a)^{n/2-\xi} p_{n/2} \qquad (B.2)$$

where the p_n are moments of the universal distribution function ϕ (see text). From the definition of s, one has $p_2/p_1 = 1$. We therefore obtain the ratios $\mathcal{M}_4/\mathcal{M}_2 = s/a$, and $\mathcal{M}_6/\mathcal{M}_4 = (s/a)(p_3/p_2)$. The ratio we seek to calculate, p_2/p_3, is then simply:

$$\frac{p_2}{p_3} = \frac{\mathcal{M}_4^2}{\mathcal{M}_2 \mathcal{M}_6}. \qquad (B.3)$$

We note that D is proportional to r. Since the ratio we wish to calculate is dimensionless, the moments of the D distribution may also be used in equation B.3: the prefactor linking D and r does not appear in the end result. Using this equation, we have calculated p_2/p_3 from the experimental particle span distributions presented in section 2, and the ratio is found to be 0.44 ± 0.02.

Appendix C

Using the complete fitted function for $\mathcal{F}$ to derive r_{av} and M_2

Here we give details for obtaining r_{av} from the dual wavelength ratio β and the wavenumbers k_1 and k_2, using our fitted form factor $\mathcal{F}$. Since $\beta = \mathcal{F}(2k_1 r_{av})/\mathcal{F}(2k_2 r_{av})$ and given our fitted form factor (4.38), we set $\varsigma = 4r_{av}^2$ and hence:

$$a'\varsigma^3 + b'\varsigma^2 + c'\varsigma + d' = 0 \tag{C.1}$$

where

$$
\begin{aligned}
a' &= c_1 c_2 k_1^2 k_2^2 (\beta k_1^2 - k_2^2) & \text{(C.2)} \\
b' &= c_2(\beta k_1^4 - k_2^4) & \text{(C.3)} \\
c' &= c_1(\beta k_2^2 - k_1^2) + & \text{(C.4)} \\
&\quad + \left(c_1 + \frac{1}{3}\right)(\beta k_1^2 - k_2^2) & \text{(C.5)} \\
d' &= \beta - 1 & \text{(C.6)}
\end{aligned}
$$

Equation C.1 is a cubic in ς, and may be solved by standard methods [see for example Press et al (1992)]. From this, one can obtain $r_{av} = \sqrt{\varsigma/4}$, and hence $\sum m^2 = \eta \lambda^4 / c\mathcal{F}(2kr_{av})$.

Bibliography

Abraham FF, 1970: Functional dependence of drag coefficient of a sphere on Reynolds number. *Phys. Fluids* **13** 2194

Ball RC *et al* , 1987: Universal kinetics in reaction-limited aggregation. *Phys. Rev. Lett.* **58** 274

Ball RC and Somfai E, 2002: A theory of diffusion controlled growth. *Phys. Rev. Lett.* **89** 135503

Ball RC and Somfai E, 2003: Diffusion controlled growth - theory and closure approximations *Phys. Rev. E* **67** 021401

Ball RC and Witten TA, 1984: Causality bound on the density of aggregates. *Phys. Rev. A* **29** 2966

Barthazy E and Schefold R, 2004: Properties of snowflakes of different riming degree and crystal types. *Proc. 14th ICCP conference, Bologna.*

Bentley WA and Humphreys WJ, 1962: *Snow Crystals.* Dover Publications.

Bergeron T, 1950: Über der mechanismus der ausgiebigen Niederschläge. *Ber. Deut. Wetterd.* **12** 225

Berry MV and Percival IC, 1986: Optics of fractal clusters such as smoke. *Opt. Acta* **33** 577

Bohren CF and Huffman DR, 1983: *Absorption and scattering of light by small particles.* Wiley, New York.

Brown WD and Ball RC, 1985: Computer simulation of chemically-limited aggregation. *J. Phys. A: Math. Gen.* **18** L517

Chandrasekhar S, 1943: Stochastic problems in physics and astronomy. *Rev. Mod.*

Phys. **15** 1 (pages 59-63)

Cueille S and Sire C, 1997: Non-trivial polydispersity exponents in aggregation models. *Phys. Rev. E* **55** 5465

Drake RL, 1972: A general mathematical survey of the coagulation equation, in *Topics in current aerosol research* eds. Hidy GM and Brock JR, Pergamon, New York.

Field PR, 1999: Aircraft observations of ice crystal evolution in an altostratus cloud. *J. Atmos. Sci.* **56** 1925

Field PR and Heymsfield AJ, 2003: Aggregation and scaling of ice crystal size distributions *J. Atmos. Sci.* **60** 544

Foot J, 1988: Some observations of the optical properties of clouds II - Cirrus. *Q. J. R. Met. Soc.* **114** 145

Forrest SR and Witten, 1979: Long-range correlations in smoke-particle aggregates. *J. Phys. A* **12** L109

Foster TC and Hallett J, 2002: The alignment of ice crystals in changing electric fields. *Atmos. Res.* **62** 149

Goldstein H, 1980: *Classical Mechanics.* Addison-Wesley, London.

Goold NR, 2004 — private communication.

Goold NR, Ball RC and Somfai E, 2004: Anisotropic diffusion limited aggregation in three dimensions - universality and non-universality. *(to be submitted to Phys. Rev. E)*

Guinier A, 1939: La diffraction des rayons X aux trespetits angles: application a l'etude de phenomes ultramicroscopiques. *Ann. Phys.* **12** 161

Guinier A *et al* , 1955: *Small angle scattering of X-rays.* Wiley, New York.

Gunn KLS and Marshall JS, 1958: The distribution with size of aggregate snowflakes *J. Meteor.* **15** 452

Hallett J *et al* , 2002: Ice crystals in Cirrus, in *Cirrus* eds. Lynch DK, Sassen K, Starr DO'C and Stephens G, Oxford University Press, New York.

Heymsfield AJ and McFarquhar GM, 2002: Midlatitude and tropical cirrus - microphysical properties, in *Cirrus* eds. Lynch DK, Sassen K, Starr DO'C and

Stephens G, Oxford University Press, New York.

Heymsfield AJ *et al* , 2002: A general approach for deriving the properties of Cirrus and Stratiform ice cloud particles *J. Atmos. Sci.* **59** 3

Hogan RJ and Illingworth AJ, 2000: Measuring crystal size in Cirrus using 35- and 94- Ghz radars *J. Atmos. & Ocean. Tech.* **17** 27

Houghton JT, 2001: *Intergovernmental panel on climate change - climate change 2001: the scientific basis.* Cambridge University Press, New York.

Jackson JD, 1975: *Classical electrodynamics.* Wiley, New York.

Jiusto JE and Weickmann HK, 1973: Types of snowfall. *Bull. Am. Met. Soc.* **54** 1148

Kiorboe T, 2001: Formation and fate of marine snow: small-scale processes with large-scale implications *Sci. Mar.* **65** 57

Kolb M *et al* , 1983: Scaling of kinetically growing clusters. *Phys. Rev. Lett.* **51** 1123

Korolev A and Isaac G, 2003: Roundness and aspect ratio of particles in ice clouds. *J. Atmos. Sci.* **60** 1795

Langer JS, 1980: Instabilities and pattern formation in crystal growth. *Rev. Mod. Phys.* **62** 1

Lee MH, 2000: On the validity of the coagulation equation and the nature of runaway growth. *Icarus* **143** 74

Lin MY *et al* , 1990: Universal reaction-limited colloid aggregation *Phys. Rev. A* **41** 2005

Liou KN, 1986: Influence of cirrus clouds on weather and climate processes: a global perspective. *Mon. Weath. Rev.* **114** 1167

Liu CJ and Illingworth AJ, 1997: Error analysis of backscatter from discrete dipole approximation for different ice particle shapes *Atmos. Res.* **44** 231

Locatelli JD and Hobbs PV, 1974: Fall speeds and masses of solid precipitation particles *J. Geophys. Res.* **79** 2185

Lucchin F, 1986: Clustering in the universe - in *Fractals in Physics*, eds. Pietronero L and Tosatti E, North-Holland, Amsterdam.

Matrosov SY, 1992: Radar reflectivity in snowfall *IEEE Trans. Geosci. & Rem. Sens.* **30** 454

Matrosov SY, 1998: A dual wavelength method to measure snowfall rate *J. App. Meteor.* **37** 1510

Maxwell-Garnett JC, 1904: Colours in metal glasses and metallic films *Phil. Trans. Roy. Soc.* **A203** 385

McDonald JE, 1954: The shape and aerodynamics of large raindrops *J. Meteor.* **11** 478

Meakin P, 1983: Formation of fractal clusters and networks by irreversible diffusion limited aggregation. *Phys. Rev. Lett.* **51** 1119

Meakin P, 1984: Computer-simulation of cluster cluster aggregation using linear trajectories - results from 3-dimensional simulations and a comparison with aggregates formed using brownian trajectories *J. Coll. & Interf. Sci.* **102** 505

Meakin P, 1999: A historical introduction to computer models for fractal aggregates *J. Sol-Gel Sci. & Tech.* **15** 2

Mie G, 1908: Beitrge zur Optik trber Medien, speziell kolloidaler Metallsungen. *Ann. Physik* **4** 377

Mitchell DL, 1983: Use of mass- and area- dimensional power laws for determining precipitation particle terminal velocities. *J. Atmos. Sci.* **53** 1710

Mitchell JFB, 1989: CO_2 and climate: a missing feedback? *Nature* **341** 132

Niemeyer L *et al* , 1984: Fractal dimension of dielectric breakdown *Phys. Rev. Lett.* **52** 1033

Passarelli RE and Srivastava, 1979: Theoretical and observational study of snow size spectra and snowflake aggregation efficiencies *J. Atmos. Sci.* **35** 882

Prupacher HR and Klett JD, 1997: *Microphysics of clouds and precipitation (2nd Ed.)*, Kluwer.

Richardson LF, 1961: in *General systems yearbook* **6** 139

Rogers RR and Yau MK, 1989: *A short course in cloud physics (3rd Ed.)*, Butterworth-Heinemann.

von Smoluchowski M, 1917: Versuch einer mathematischen theorie der koagula-

tionskinetik kolloider losungen. *Phys. Chem.* **92** 129

Sasyo Y and Matsuō T, 1985: *J. Met. Soc. Jap.* **63** 249

Sorensen CM, 2001: Light scattering by fractal aggregates: a review. *Aerosol Sci. & Tech.* **35** 648

Stanley HE, 1986: Form: an introduction to self-similarity and fractal behaviour, in *On growth and form* eds. Stanley HE and Ostrowsky N, Martinus Nijhoff, Dordrecht.

Stephens GL, 1990: The relevance of the microphysical and radiative transfer properties of cirrus clouds to climate and climatic feedback. *J. Atmos. Sci.* **47** 1742

Tomotika S, 1935: The laminar boundary layer on the surface of a sphere in a uniform stream. *Report and memo, Great Britain Aeronautical Research Committee* 1678 14pp. HMSO, London.

Van Dongen PGJ 1987a: On the possible occurence of instantaneous gelation in Smoluchowski's coagulation equation. *J. Phys. A: Math. Gen.* **20** 1889

Van Dongen PGJ 1987b: Solutions of Smoluchowski's equations at large cluster sizes*Physica A* **145** 15

Van Dongen PGJ and Ernst MH, 1985: Dynamical scaling in the kinetics of clustering. *Phys. Rev. Lett.* **54** 13

Van Dongen PGJ and Ernst MH, 1986: Tail distribution for large clusters in irreversible aggregation, in *Fractals in Physics* eds. Pietronero L and Tosatti E

Van Dongen PGJ and Ernst MH, 1987: Tail distribution of large clusters from the coagulation equation. *J. Colloid & Interface Sci.* **115** 27

Vicsek T, 1989: *Fractal growth phenomena.* World Scientific Publishing, London.

Westbrook CD, Ball RC, Field PR and Heymsfield AJ, 2004a: Universality in snowflake aggregation. *Geophys. Res. Lett.* **31** L15104

Westbrook CD, Ball RC, Field PR and Heymsfield AJ, 2004b: A theory of growth by differential sedimentation, with application to snowflake formation. *Phys. Rev. E* **70** 021403

White WH, 1980: A global existence theorem for Smoluchowski's coagulation

equations. *Proc. Am. Math. Soc.* **80** 273i

Witten TA and Sander LM, 1981: Diffusion-limited aggregation: a kinetic critical phenomenon. *Phys. Rev. Lett.* **47** 1400

Witten TA and Sander LM, 1983: Diffusion-limited aggregation. *Phys. Rev. B* **27** 5686

Ziff RM, 1984: Aggregation kinetics via Smoluchowski's equation, in *Kinetics of aggregation and gelation* eds. Family F and Landau DP, North-Holland, Amsterdam.